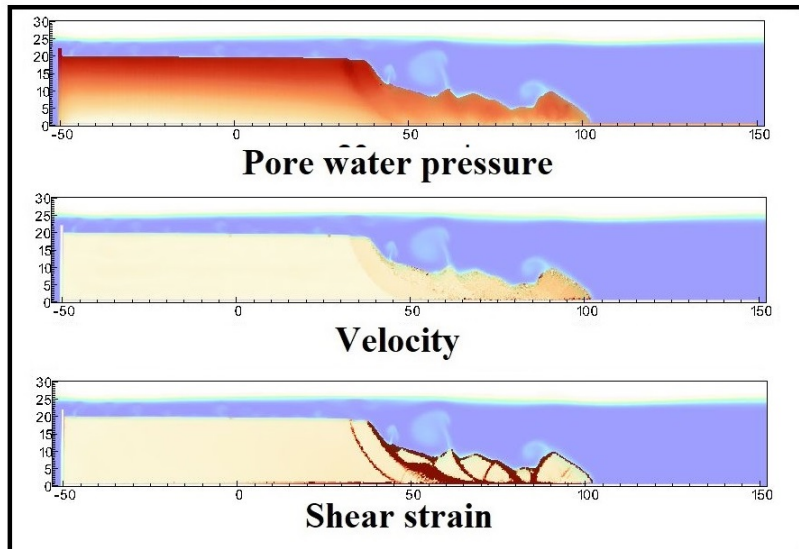


- 1 Graphical Abstract
- 2 MPMICE: A hybrid MPM-CFD model for simulating coupled problems in porous media. Application to earthquake-induced submarine landslides
- 3 Quoc Anh Tran, Gustav Grimstad, Seyed Ali Ghoreishian Amiri



Application to earthquake-induced submarine landslide

₆ Highlights

₇ **MPMICE: A hybrid MPM-CFD model for simulating coupled prob-**
₈ **lems in porous media. Application to earthquake-induced subma-**
₉ **rine landslides**

₁₀ Quoc Anh Tran, Gustav Grimstad, Seyed Ali Ghoreishian Amiri

- ₁₁ • MPMICE is introduced for multiphase flow in porous media.
- ₁₂ • Material Point method allows to model large deformation of non-isothermal
- ₁₃ porous media.
- ₁₄ • ICE (compressible multi-material CFD formulation) allows stabilizing
- ₁₅ pore water pressure and turbulent flow.
- ₁₆ • MPMICE is validated and apply to simulate the earthquake-induced
- ₁₇ submarine landslide.

¹⁸ MPMICE: A hybrid MPM-CFD model for simulating
¹⁹ coupled problems in porous media. Application to
²⁰ earthquake-induced submarine landslides

²¹ Quoc Anh Tran^a, Gustav Grimstad^a, Seyed Ali Ghoreishian Amiri^a

^a*Norwegian University of Science and Technology, , Trondheim, 7034, Norway*

²² Abstract

²³ In this paper, we describe a soil-fluid-structure interaction model that com-
²⁴ bines soil mechanics (saturated sediments), fluid mechanics (seawater or air),
²⁵ and solid mechanics (structures). The formulation combines the Material
²⁶ Point Method, which models large deformation of the porous media and the
²⁷ structure, with the Implicit Continuous-fluid Eulerian, which models com-
²⁸ plex fluid flows. We validate the model and simulate the whole process of
²⁹ earthquake-induced submarine landslides. We show that this model captures
³⁰ complex interactions between saturated sediment, seawater, and structure,
³¹ so we can use the model to estimate the impact of potential submarine land-
³² slides on offshore structures.

³³ *Keywords:*

³⁴ Material Point Method, MPMICE, submarine landslide.

35	Contents	
36	Nomenclature	4
37	Introduction	6
38	Theory and formulation	8
39	Assumptions	8
40	Governing equations	9
41	Constitutive soil model	11
42	Turbulent model	12
43	Frictional force for soil-structure interaction	12
44	Momentum and Energy exchange model	13
45	Solving momentum and energy exchange with an implicit solver	14
46	Equation of state for fluid phases	16
47	Numerical implementation	17
48	Interpolation from Solid Particle to Grid	18
49	Compute equation of state for fluid phase	20
50	Compute cell face velocity	20
51	Compute cell face temperature	21
52	Compute fluid pressure (implicit scheme)	22
53	Compute viscous shear stress term of the fluid phase	22
54	Compute nodal internal temperature of the solid phase	22
55	Compute and integrate acceleration of the solid phase	23
56	Compute Lagrangian value (mass, momentum and energy)	23
57	Compute Lagrangian specific volume of the fluid phase	24
58	Compute advection term and advance in time	25
59	Interpolate from cell to node of the solid phase	26
60	Update the particle variables	26
61	Numerical examples	27
62	Fluid Flow through isothermal porous media	27
63	Isothermal consolidation	28
64	Thermal induced cavity flow	29
65	Underwater debris flow	30
66	Earthquake-induced submarine landslides	34
67	Conclusions	38

68	Acknowledgements	39
69	Appendix: Equation derivation	39
70	Evolution of porosity	39
71	Momentum conservation	40
72	Energy conservation	41
73	Advanced Fluid Pressure	42
74	Momentum and Energy exchange with an implicit solver	43

⁷⁵ **Nomenclature**

General variables

<u>Variable</u>	<u>Dimensions</u>	<u>Description</u>
V	$[L^3]$	Representative volume
n		Porosity
σ	$[ML^{-1}t^{-2}]$	Total stress tensor
Δt	$[t]$	Time increment
\mathbf{b}	$[ML^1t^{-2}]$	Body force
c_v	$[L^2t^{-2}T^{-1}]$	Constant volume specific heat
f_d	$[MLt^{-2}]$	Drag forces in momentum exchange term
f^{int}	$[MLt^{-2}]$	Internal forces
f^{ext}	$[MLt^{-2}]$	External forces
q_{fs}	$[MLt^{-2}]$	Heat exchange term
S		Weighting function
∇S		Gradient of weighting function

⁷⁶

Solid phase

<u>Variable</u>	<u>Dimensions</u>	<u>Description</u>
m_s	$[M]$	Solid mass
ρ_s	$[ML^{-3}]$	Solid density
ϕ_s		Solid volume fraction
$\bar{\rho}_s$	$[ML^{-3}]$	Bulk Solid density
\mathbf{x}_s	$[L]$	Solid Position vector
\mathbf{U}_s	$[Lt^{-1}]$	Solid Velocity vector
\mathbf{a}_s	$[Lt^{-2}]$	Solid Acceleration vector
σ'	$[ML^{-1}t^{-2}]$	Effective Stress tensor
ϵ_s		Strain tensor
e_s	$[L^2t^{-2}]$	Solid Internal energy per unit mass
T_s	$[T]$	Solid Temperature
\mathbf{F}_s		Solid Deformation gradient
V_s	$[L^3]$	Solid Volume

⁷⁷

Fluid phase

<u>Variable</u>	<u>Dimensions</u>	<u>Description</u>
m_f	[M]	Fluid mass
ρ_f	[ML ⁻³]	Fluid density
ϕ_f		Fluid volume fraction
$\bar{\rho}_f$	[ML ⁻³]	Bulk Fluid density
\mathbf{U}_f	[Lt ⁻¹]	Fluid Velocity vector
$\boldsymbol{\sigma}_f$	[ML ⁻¹ t ⁻²]	Fluid stress tensor
p_f	[ML ⁻¹ t ⁻²]	Fluid isotropic pressure
$\boldsymbol{\tau}_f$	[ML ⁻¹ t ⁻²]	Fluid shear stress tensor
e_f	[L ² t ⁻²]	Fluid Internal energy per unit mass
T_f	[T]	Fluid Temperature
v_f	[L ³ /M]	Fluid Specific volume $\frac{1}{\rho_f}$
α_f	[1/T]	Thermal expansion
μ	[ML ⁻¹ t ⁻¹]	Fluid viscosity
V_f	[L ³]	Fluid Volume

Superscript

<u>Variable</u>	<u>Dimensions</u>	<u>Description</u>
n		Current time step
L		Lagrangian values
$n + 1$		Next time step

Subscript

c	Cell-centered quantity
p	Particle quantity
i	Node quantity
FC	Cell face quantity
L, R	Left and Right cell faces

78 **Introduction**

79 Many geological natural processes and their interactions with man-made
80 structures are influenced by soil-fluid-structure interactions. The prediction
81 of these processes requires a tool that can capture complex interactions
82 between soil, fluid, and structure, such as the process of submarine land-
83 slides. Indeed, The offshore infrastructure as well as coastal communities
84 may be vulnerable to submarine landslides. Submarine landslides contain
85 three stages: triggering, failure, and post-failure. Erosion or earthquakes can
86 trigger slope failures in the first stage. Following the failure, sediments move
87 quickly after the post-failure stage. In other words, solid-like sediments will
88 behave like a fluid after failure. This phase transition makes the simulation
89 of submarine landslides a challenging task.

90
91 Due to this phase transition, submarine landslide can be modeled by ei-
92 ther the Computational Fluid Dynamics (CFD) or the particle-based meth-
93 ods. For simulating submarine slides, CFD methods solve governing equa-
94 tions in a full-Eulerian framework [1, 2, 3, 4] with interface capturing tech-
95 niques. While CFD can handle complex flows (such as turbulent flows), it
96 cannot account for the triggering mechanism of submarine landslides because
97 it is not straightforward to consider 'soil constitutive laws' of sediment ma-
98 terials in the Eulerian framework. In contrast, particle-based methods can
99 overcome this problem by using the Lagrangian framework. These meth-
100 ods have been extensively used to simulate landslides, like Material Point
101 Method (MPM) [5], Smooth Particle Hydro Dynamics [6], Particle Finite
102 Element Method [7], or Coupled Eulerian Lagrangian Method [8]. For sim-
103 plicity, these simulations adopt total stress analysis which neglects the pore
104 pressure development which is key factor triggering slope failures.

105
106 Recent developments in particle-based methods model the coupling of
107 fluid flows in porous media by sets of Lagrangian particles. For the MPM
108 family, it is the double-point MPM ([9, 10, 11]) where fluid particles and
109 solid particles are overlapped in a single computational grid. Even if fluid
110 flows are considered, particle-based methods have numerical instability in
111 modeling the fluid flow, which requires additional numerical treatments such
112 as the B-bar method [9], null-space filter [12], or least square approximation
113 [13, 14]. Indeed, CFD is a more optimal option for complex fluid flows
114 especially dealing with large distortions of continuum fluid media. Therefore,

115 it could be ideal to combine the CFD with particle-based methods. More than
 116 50 particle-based methods have been developed to solve large deformations
 117 of solids over the last two decades [15], but the MPM appears to be the
 118 best candidate for coupling with the CFD. Because MPM incorporates a
 119 stationary mesh during computation, just like CFD. As such, both MPM
 120 and CFD can be coupled naturally in a unified computational mesh.



Figure 1: Interaction between soil-fluid-structure

121

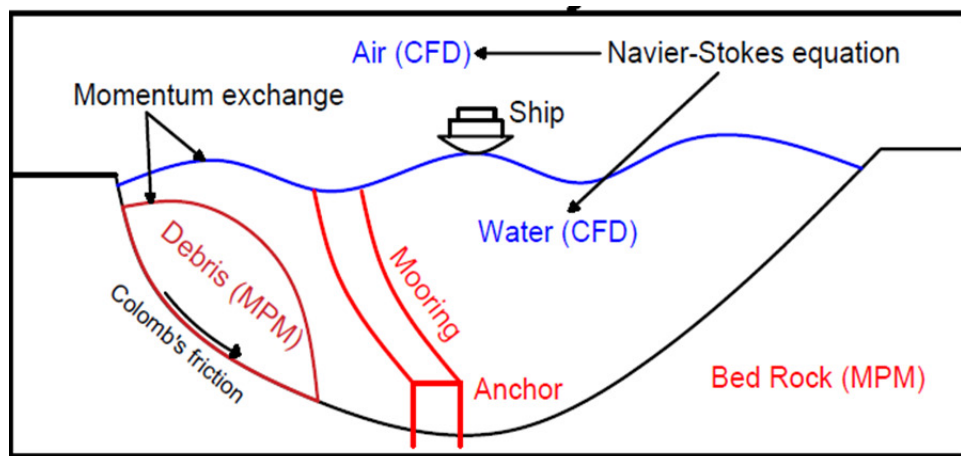


Figure 2: Coupling of soil-water-structure interaction using MPMICE

122 A numerical method for simulating soil-fluid-structure interaction (Figure
123 1) involving large deformations, is presented in this work in order to simu-
124 late the interaction between sediment (soil), seawater (fluid) and offshore
125 structures (structure) namely MPMICE (Figure 2). In the MPMICE, the
126 Material Point Method (MPM) is coupled with the Implicit Continuous Eu-
127 lerian (ICE). The MPM method is a particle method that allows the porous
128 soil to undergo arbitrary distortions. The ICE method, on the other hand,
129 is a conservative finite volume technique with all state variables located at
130 the cell center (temperature, velocity, mass, pressure). An initial technical
131 report [16] at Los Alamos National Laboratory provided the theoretical and
132 algorithmic foundation for the MPMICE, followed by the MPMICE devel-
133 opment and implementation in the high-performance Uintah computational
134 framework for simulating fluid-structure interactions [17]. This paper pri-
135 marily contributes further to the development of the MPMICE for analyzing
136 the **soil**-fluid-structure interaction, since sediment should be considered as a
137 porous media (soil) and not as a solid to capture the evolution of the pore
138 water pressure. Baumgarten et al. [18] made the first attempt at coupling
139 the Finite Volume Method with the MPM for the simulation of soil-fluid
140 interaction. In contrast to the mentioned work, we use implicit time integra-
141 tion for the multi phase flows instead of explicit time integration for the
142 single-phase flow.

143 **Theory and formulation**

144 This section lay out the theoretical framework for the MPMICE model.
145 We use the common notation of the continuum mechanics with vector and
146 tensor denoted simply by using bold font and scalar denoted by using normal
147 font. The notation are shown in Nomenclature.

148 *Assumptions*

149 The following assumptions are made for the MPMICE model.

- 150 1. Solid phases (MPM) are described in a Lagrangian formulation while
151 fluid phases (ICE) are described in an Eulerian formulation in the
152 framework of continuum mechanics and mixture theory.
- 153 2. Solid grains are incompressible while the fluid phases are compressible.
154 Solid's thermal expansion is negligible.
- 155 3. There is no mass exchange between solid and fluid phases.
- 156 4. Terzaghi's effective stress is valid.

157 *Governing equations*

158 A representative element volume Ω is decomposed by two domains: solid
159 domains Ω_s and fluid domains Ω_f . Then, all domains are homogenized
160 into two overlapping continua. Considering the volume fraction of solid
161 $\phi_s = \Omega_s/\Omega$ and fluid $\phi_f = \Omega_f/\Omega$ with the true (or Eulerian) porosity
162 $n = \sum \phi_f$ of the representative element volume, the average density of solid
163 and fluid phases are defined as:

164

$$\bar{\rho}_s = \phi_s \rho_s, \quad \bar{\rho}_f = \phi_f \rho_f \quad (1)$$

165 The mass of solid and fluid phases are:

166

$$m_s = \int_{\Omega_s} \rho_s dV = \bar{\rho}_s V, \quad m_f = \int_{\Omega_f} \rho_f dV = \bar{\rho}_f V \quad (2)$$

167 Reviewing the Terzaghi's effective stress concept for the saturated porous
168 media, the total stress $\boldsymbol{\sigma}$ is calculated by:

169

$$\boldsymbol{\sigma} = \boldsymbol{\sigma}' - p_f \mathbf{I} \quad (3)$$

170 The balance equations are derived based on the mixture theory. The rep-
171 resentative thermodynamic state of the fluid phases are given by the vector
172 $[m_f, \mathbf{U}_f, e_f, T_f, v_f]$ which are mass, velocity, internal energy, temperature,
173 specific volume. The representative state of the solid phases are given by the
174 vector $[m_s, \mathbf{U}_s, e_s, T_s, \boldsymbol{\sigma}', p_f]$ which are mass, velocity, internal energy, temper-
175 ature, effective stress and pore water pressure. The derivation is presented
176 in detail in the Appendix.

177

178 Mass Conservation

179 The mass balance equations for both fluid (e.g., water, air) and solid phases
180 are:

181

$$\frac{1}{V} \frac{\partial m_f}{\partial t} + \nabla \cdot (m_f \mathbf{U}_f) = 0, \quad \frac{1}{V} \frac{D_s m_s}{Dt} = 0 \quad (4)$$

182 Solving the mass balance equation leads to:

$$\frac{D_s n}{Dt} = \phi_s \nabla \cdot \mathbf{U}_s \quad (5)$$

183

184 Momentum Conservation

¹⁸⁵ The momentum balance equations for the fluid phases (e.g., water, air) are:

$$\frac{1}{V} \left[\frac{\partial(m_f \mathbf{U}_f)}{\partial t} + \nabla \cdot (m_f \mathbf{U}_f \mathbf{U}_f) \right] = -\phi_f \nabla p_f + \nabla \cdot \boldsymbol{\tau}_f + \bar{\rho}_f \mathbf{b} + \sum \mathbf{f}_d \quad (6)$$

¹⁸⁶ The momentum balance equations for the solid phases are:

$$\frac{1}{V} \frac{D_s(m_s \mathbf{U}_s)}{Dt} = \nabla \cdot (\boldsymbol{\sigma}') - \phi_s \nabla p_f + \bar{\rho}_s \mathbf{b} + \sum \mathbf{f}_{fric} - \sum \mathbf{f}_d \quad (7)$$

¹⁸⁷

¹⁸⁸ Energy Conservation

¹⁸⁹ The internal energy balance equations for the fluid phases (e.g., water, air)
¹⁹⁰ are:

$$\frac{1}{V} \left[\frac{\partial(m_f e_f)}{\partial t} + \nabla \cdot (m_f e_f \mathbf{U}_f) \right] = -\bar{\rho}_f p_f \frac{D_f v_f}{Dt} + \boldsymbol{\tau}_f : \nabla \mathbf{U}_f + \nabla \cdot \mathbf{q}_f + \sum q_{sf} \quad (8)$$

¹⁹¹ The internal energy balance equations for the solid phase are:

$$\frac{m_s}{V} c_v \frac{D_s(T_s)}{Dt} = \boldsymbol{\sigma}' : \frac{D_s(\boldsymbol{\epsilon}_s^p)}{Dt} + \nabla \cdot \mathbf{q}_s - \sum q_{sf} \quad (9)$$

¹⁹² where c_v is the specific heat at constant volume of the solid materials.

¹⁹³

¹⁹⁴ Closing the systems of equations, the following additional models are needed:

¹⁹⁵ (1) A constitutive equation to describe the stress - strain behaviour of solid
¹⁹⁶ phase (computing effective stress $\boldsymbol{\sigma}'$).

¹⁹⁷ (2) Optional turbulent model to compute the viscous shear stress $\boldsymbol{\tau}_f$.

¹⁹⁸ (3) Frictional forces \mathbf{f}_{fric} for the contact for soil-structure interaction be-
¹⁹⁹ tween solid/porous materials with the friction coefficient μ_{fric} .

²⁰⁰ (4) Exchange momentum models (computing drag force \mathbf{f}_d) for interaction
²⁰¹ between materials.

²⁰² (5) Energy exchange models (computing temerature exhangre term q_{sf}) for
²⁰³ interaction between materials.

²⁰⁴ (6) An equation of state to establish relations between thermodynamics vari-
²⁰⁵ ables of each fluid materials $[P_f, \bar{\rho}_f, v_f, T_f, e_f]$.

²⁰⁶ Four thermodynamic relations for the equation of states are:

$$\begin{aligned} e_f &= e_f(T_f, v_f) \\ P_f &= P_f(T_f, v_f) \\ \phi_f &= v_f \bar{\rho}_f \\ 0 &= n - \sum_{f=1}^{N_f} v_f \bar{\rho}_f \end{aligned} \quad (10)$$

²⁰⁷ *Constitutive soil model*

²⁰⁸ As a result of the explicit MPM formulation, we can derive the constitutive law in the updated Lagrangian framework of "small strain - large deformation". Therefore, the rotation of the particles (representative element volume) is manipulated by rotating the Cauchy stress tensor. First, the deformation gradient is decomposed into the polar rotation tensor \mathbf{R}_s^{n+1} and stretch tensor \mathbf{V}_s^{n+1} as:

$$\mathbf{F}_s^{n+1} = \mathbf{V}_s^{n+1} \mathbf{R}_s^{n+1} \quad (11)$$

²¹⁴ Then, before calling the constitutive model, the stress and strain rate tensor are rotated to the reference configuration as:

$$\boldsymbol{\sigma}'^{n*} = (\mathbf{R}_s^{n+1})^T \boldsymbol{\sigma}'^{n*} \mathbf{R}_s^{n+1} \quad (12)$$

$$\delta\boldsymbol{\epsilon}^{n*} = (\mathbf{R}_s^{n+1})^T \delta\boldsymbol{\epsilon}_s^{n*} \mathbf{R}_s^{n+1} \quad (13)$$

²¹⁷ Using the constitutive model with the input tensors $\boldsymbol{\sigma}'^{n*}, \delta\boldsymbol{\epsilon}^{n*}$ to compute the Cauchy stress tensor at the advanced time step $\boldsymbol{\sigma}'^{n+1*}$ then rotating it back to current configuration as:

$$\boldsymbol{\sigma}'^{n+1} = \mathbf{R}_s^{n+1} \boldsymbol{\sigma}'^{n+1*} (\mathbf{R}_s^{n+1})^T \quad (14)$$

²²⁰ In this paper, we adopt the hyper-elastic Neo Hookean model for the structure materials and additionally Mohr-Coulomb failure criteria for the soil (porous media) materials. The Cauchy stress of the hyper-elastic Neo Hookean model can be written as:

$$\boldsymbol{\sigma}' = \frac{\lambda \ln(J)}{J} + \frac{\mu}{J} (\mathbf{F} \mathbf{F}^T - \mathbf{J}) \quad (15)$$

²²⁴ where λ and μ are bulk and shear modulus ad J is the determinant of the deformation gradient \mathbf{F} . And the yield function f and flow potentials g of

²²⁶ the Mohr-Coulomb can be written as:

$$\begin{aligned} f &= \sigma'_1 - \sigma'_3 - 2c' \cos(\phi') - (\sigma'_1 + \sigma'_3) \sin(\phi') \\ g &= \sigma'_1 - \sigma'_3 - 2c' \cos(\psi') - (\sigma'_1 + \sigma'_3) \sin(\psi') \end{aligned} \quad (16)$$

²²⁷ where the c' , ϕ' and ψ' are cohesion and friction angle and dilation angle. σ'_1
²²⁸ and σ'_3 are maximum and minimum principal stress.

²²⁹ *Turbulent model*

²³⁰ The turbulent effect is modelled using a statistical approach namely large-
²³¹ eddy simulation. In this approach, the micro-scale turbulent influence in the
²³² dynamics of the macro-scale motion is computed through simple models like
²³³ Smagorinsky model. In the Smagorinsky model, the residual stress tensor is:

$$\tau_{ij} = 2\mu_{eff}(\bar{S}_{ij} - \frac{1}{3}\delta_{ij}\bar{S}_{kk}) + \frac{1}{3}\delta_{ij}\tau_{kk} \quad (17)$$

²³⁴ where the strain rate tensor is given by:

$$\bar{S}_{ij} = \frac{1}{2}(\frac{\delta \bar{U}_i}{\delta x_j} + \frac{\delta \bar{U}_j}{\delta x_i}) \quad (18)$$

²³⁵ and the effective viscosity is sum of molecular viscosity and turbulent viscosity
²³⁶ $\mu_{eff} = \mu + \mu_t$ in which the turbulent viscosity μ_t is calculated by:

$$\mu_t = (C_s \Delta)^2 \sqrt{2\bar{S}_{ij}\bar{S}_{ij}} \quad (19)$$

²³⁷ where C_s is the Smagorinsky constant with the value of 0.1 and $\Delta = \sqrt[3]{dxdydz}$
²³⁸ is the grid size that defines the subgrid length scale.

²³⁹ *Frictional force for soil-structure interaction*

²⁴⁰ MPMICE includes a contact law for the interaction between soil and
²⁴¹ structure using the first Coulomb friction contact for MPM presented by
²⁴² Bardenhagen et al. ([19]). The magnitude of the friction force at the contact
²⁴³ depends on the friction coefficient μ_{fric} and the normal force \mathbf{f}_{norm} computed
²⁴⁴ from the projection of the contact force in the normal direction.

$$\mathbf{f}_{fric} = \mu_{fric} \mathbf{f}_{norm} \quad (20)$$

245 The contact determines whether the soil is sliding or sticking to the structure
 246 by comparing the friction force with the sticking force \mathbf{f}_{stick} computed from
 247 the projection of the contact force in the tangent direction as:

$$\begin{aligned} \text{if } \mathbf{f}_{fric} \geq \mathbf{f}_{stick} & \text{ no sliding} \\ \text{if } \mathbf{f}_{fric} < \mathbf{f}_{stick} & \text{ sliding occurs} \end{aligned} \quad (21)$$

248 Frictional sliding between solid materials also generates dissipation and the
 249 work rate generated from the sliding can be calculated as:

$$\Delta W_{friction} = \mathbf{f}_{fric} d \quad (22)$$

250 where d is the sliding distance which can be computed based on the sliding
 251 velocity between two materials.

252 *Momentum and Energy exchange model*

253 Currently, the energy exchange coefficient H_{sf} is assumed to be constant
 254 for the sake of simplicity. Then the energy exchange can be written as:

$$q_{sf} = H_{sf}(T_f - T_s) \quad (23)$$

255 On the other hand, the drag force can be calculated as:

$$f_d = K(\mathbf{U}_s - \mathbf{U}_f) \quad (24)$$

256 For the momentum exchange between fluid flows and porous media, we as-
 257 sume that the drag force \mathbf{f}_d depends on the average grain size of the grains
 258 D_p , the porosity n , the fluid viscosity μ_f , and is proportional to the relative
 259 velocities of soil grains and fluid $(\mathbf{U}_s - \mathbf{U}_f)$. Based on recent investigation
 260 of CFD simulations of fluid flow around mono- and bi-disperse packing of
 261 spheres for $0.1 < \phi_s < 0.6$ and $Re < 1000$ [20]. The drag force is given by:

$$\mathbf{f}_d = \frac{18\phi_s(1-\phi_s)\mu_f}{D_p^2} F(\phi_s, Re)(\mathbf{U}_s - \mathbf{U}_f) \quad (25)$$

263 where Reynolds number Re are computed as:

$$Re = \frac{n\rho_f D_p}{\mu_f} \|(\mathbf{U}_s - \mathbf{U}_f)\| \quad (26)$$

²⁶⁴ The function $F(\phi_s, Re)$ can be calculated as:

$$F(\phi_s, Re) = F(\phi_s, 0) + \frac{0.413Re}{24(1-\phi_s)^2} \left(\frac{(1-\phi_s)^{-1} + 3\phi_s(1-\phi_s) + 8.4Re^{-0.343}}{1 + 10^{3\phi_s}Re^{-(1+4\phi_s)/2}} \right) \quad (27)$$

²⁶⁵ where the low Reynold coefficient $F(\phi_s, Re \rightarrow 0)$ is:

$$F(\phi_s, 0) = \frac{10\phi_s}{(1-\phi_s)^2} + (1-\phi_s)^2(1 + 1.5\sqrt{\phi_s}) \quad (28)$$

²⁶⁶ When validating the model with analytical solution, it requires to know the
²⁶⁷ hydraulic conductivity K . In such case, we convert the equation (29) to
²⁶⁸ Kozeny-Carman formula by assuming $F(\phi_s, Re) = 10\phi_s/(1-\phi_s)^2$, leading to

$$\mathbf{f}_d = \frac{180\phi_s^2\mu_f}{D_p^2(1-\phi_s)} (\mathbf{U}_s - \mathbf{U}_f) \quad (29)$$

²⁶⁹ Then, the draging force following the Darcy law is given by:

$$\mathbf{f}_d = \frac{n^2\mu_f}{\kappa} (\mathbf{U}_s - \mathbf{U}_f) \quad (30)$$

²⁷⁰ where κ being intrinsic permeability of soil which can be written as:

$$\kappa = \frac{K\mu_f}{\rho_f g} \quad (31)$$

²⁷¹ As such, the hydraulic conductivity will be expressed as:

$$K = \frac{D_p^2(1-\phi_s)^3}{180\phi_s^2\mu_f} \rho_f g \quad (32)$$

²⁷² *Solving momentum and energy exchange with an implicit solver*

²⁷³ The derivation of the implicit integration for the momentum exchange is
²⁷⁴ presented in the Appendix's section 'Momentum and energy exchange with
²⁷⁵ an implicit solver'. The linear equations for multi phases i,j=1:N has the
²⁷⁶ form as:

$$\begin{vmatrix} (1+\beta_{ij}) & -\beta_{ij} \\ -\beta_{ji} & (1+\beta_{ji}) \end{vmatrix} \begin{vmatrix} \Delta\mathbf{U}_i \\ \Delta\mathbf{U}_j \end{vmatrix} = \begin{vmatrix} \beta_{ij}(\mathbf{U}_i^* - \mathbf{U}_j^*) \\ \beta_{ji}(\mathbf{U}_i^* - \mathbf{U}_j^*) \end{vmatrix}$$

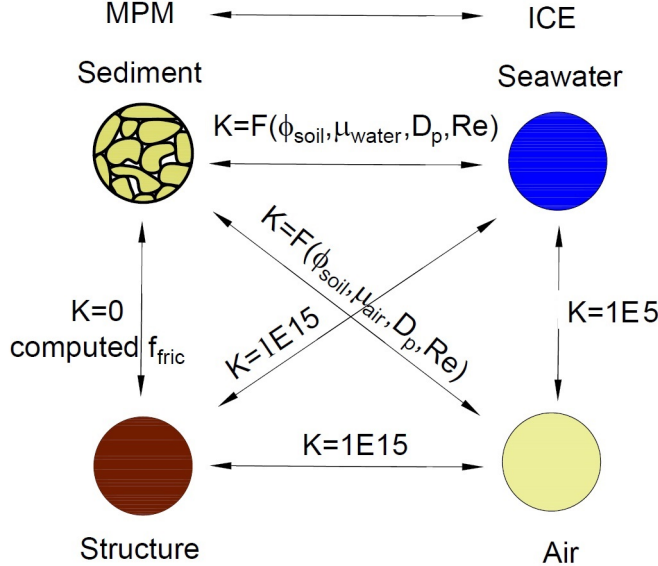


Figure 3: Momentum exchange coefficient between materials

277 where the intermediate velocity for fluid phases $f=1:N_f$ and for solid/porous
278 phases $s=1:N_s$ can be calculated by:

$$\begin{aligned} U_f^* &= U_f^n + \Delta t \left(-\frac{\nabla P_f^{n+1}}{\rho_f^n} + \frac{\nabla \cdot \tau_f^n}{\bar{\rho}_f^n} + \mathbf{b} \right) \\ U_s^* &= U_s^n + \Delta t \left(\frac{\nabla \cdot \sigma'^n}{\bar{\rho}_s^n} - \frac{\nabla P_f^{n+1}}{\rho_s} + \mathbf{b} \right) \end{aligned} \quad (33)$$

279 Also, the momentum exchange coefficient can be computed at every time
280 step as $\beta_{12} = K/\bar{\rho}_f^n$ and $\beta_{21} = K/\bar{\rho}_s^n$ with the coefficient depending on the
281 different type of interactions (see Figure 3) as for example:

282

- 283 1. The drag force is set to zero in soil-structure interactions, and instead
284 the frictional force is computed.
285 2. As a result of fluid-structure interaction, the momentum exchange coef-
286 ficient should be extremely high ($1E15$) when the solid material points
287 are considered to be zero-porosity/zero-permeability.
288 3. In the case of soil-fluid interaction, the drag force is calculated using
289 the equation (29). Considering that air has a much lower viscosity than

water, its drag force is much lower than the drag force of water in a pore.

- 292 4. A momentum exchange coefficient of 1E5 is applied between multiphase
 293 flows. This value is far higher than reality [21], but it is necessary to
 294 have enough numerical stability to conduct simulations in the numerical
 295 example.

296 Similar approach applied for the energy exchange term leading to:

$$\begin{vmatrix} (1 + \eta_{ij}) & -\eta_{ij} \\ -\eta_{ji} & (1 + \eta_{ji}) \end{vmatrix} \begin{vmatrix} \Delta T_i \\ \Delta T_j \end{vmatrix} = \begin{vmatrix} \eta_{ij}(T_i^n - T_j^n) \\ \eta_{ji}(T_j^n - T_i^n) \end{vmatrix}$$

297 with η being the energy exchange coefficient.

298 *Equation of state for fluid phases*

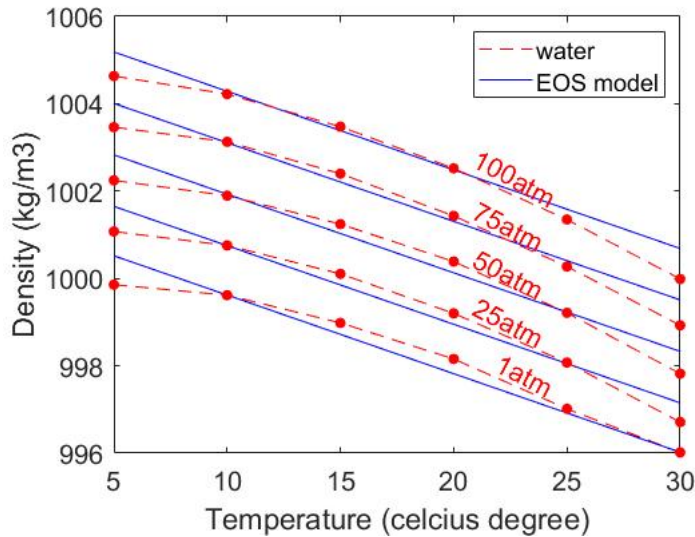


Figure 4: Equation of state of water

299 The equation of state establishes relations between thermodynamics vari-
 300 ables $[P_f, \rho_f, T_f]$. The choice of the equation of state depends on the types
 301 of the fluid materials. For example, for the air, it is possible to assume the
 302 equation of state for the perfect gas which obeys:

$$P_f = \rho_f R T_f \quad (34)$$

303 where R is the gas constant. For the water, a simple linear equation of state
 304 is in the following form:

$$P_f = P_{ref} + K_f(\rho_f - \rho_{ref} - \alpha_f(T_f - T_{ref})) \quad (35)$$

305 where reference pressure $P_{ref} = 1$ atm = 101325 Pa, reference temperature
 306 $T_{ref} = 10^\circ\text{C}$, reference density $\rho_{ref} = 999.8 \text{ kg/m}^3$, the bulk modulus of water
 307 $K_f = 2 \text{ GPa}$, and the water thermal expansion $\alpha_f = 0.18 \text{ }^\circ\text{C}^{-1}$. Equation
 308 (35) matches well with the state of the water (see Figure 4).

309 **Numerical implementation**

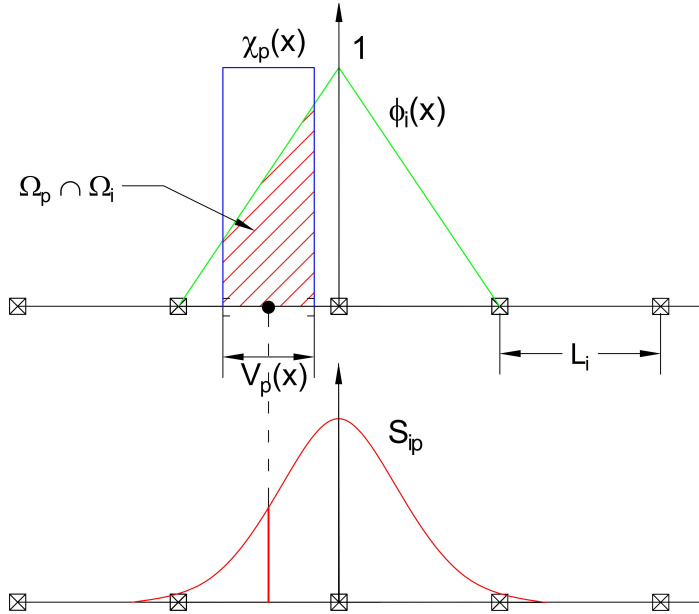


Figure 5: GIMP weighting function (red as a convolution of the linear basis shape function (green) and the characteristic function (blue))

310 The fluid phases are discretized in the grid with the state variables stored
 311 at the centroid of the cells $[\rho_{f,c}, \mathbf{U}_{f,c}, T_{f,c}, v_{f,c}]$ while the solid phase is dis-
 312 cretized in the particles with the state variables $[m_{sp}, \mathbf{U}_{sp}, T_{sp}, \boldsymbol{\sigma}'_{sp}]$. In the
 313 Material Point Method, we use the generalized interpolation technique [22]
 314 using the weight function as a convolution of a grid shape function $N_i(\mathbf{x})$ in

³¹⁵ a nodal domain Ω_i and a characteristic function $\chi_p(\mathbf{x})$ in a particle domain
³¹⁶ Ω_p with the volume $V_p(\mathbf{x})$ as follows:

$$S_{ip} = \frac{1}{V_p} \int_{\Omega_i \cap \Omega_p} N_i(\mathbf{x}) \chi_p(\mathbf{x}) d\mathbf{x} \quad (36)$$

³¹⁷ where the volume $V_p(\mathbf{x})$ of the material point p can be calculated as:

$$V_p = \int_{\Omega_p} \chi_p(\mathbf{x}) d\mathbf{x} \quad (37)$$

³¹⁸ The characteristic function is the Heaviside function as $\chi_p = 1$ if $\mathbf{x} \in \Omega_p$,
³¹⁹ otherwise 0 (see Figure 5). For the interpolation of the centroid of the cell,
³²⁰ the linear basis function is used as:

$$S_{ci} = N_i(\mathbf{x}_c) \quad (38)$$

³²¹ The time discretization are solved using the following steps.

³²² *Interpolation from Solid Particle to Grid*

³²³ The nodal values of the solid state (mass, velocity, temperature, volume)
³²⁴ are:

$$\begin{aligned} m_{si}^n &= \sum S_{ip} m_{sp} \\ \mathbf{U}_{si}^n &= \frac{\sum S_{ip} (m\mathbf{U})_{sp}^n}{m_{si}^n} \\ T_{si}^n &= \frac{\sum S_{ip} (mT)_{sp}^n}{m_{si}^n} \\ V_{si}^n &= \frac{\sum S_{ip} (mV)_{sp}^n}{m_{si}^n} \\ \boldsymbol{\sigma}_{si}^n &= \frac{\sum S_{ip} (\boldsymbol{\sigma}V)_{sp}^n}{V_{si}^n} \end{aligned} \quad (39)$$

³²⁵ The nodal internal forces is calculated by:

$$\mathbf{f}_{si}^{int,n} = - \sum \nabla S_{ip} (\boldsymbol{\sigma}'_{sp})^n V_{sp}^n \quad (40)$$

³²⁶ The nodal external forces $f_{si}^{ext,n}$ and the nodal frictional forces f_{si}^{fric} from
³²⁷ contact between materials are computed here.

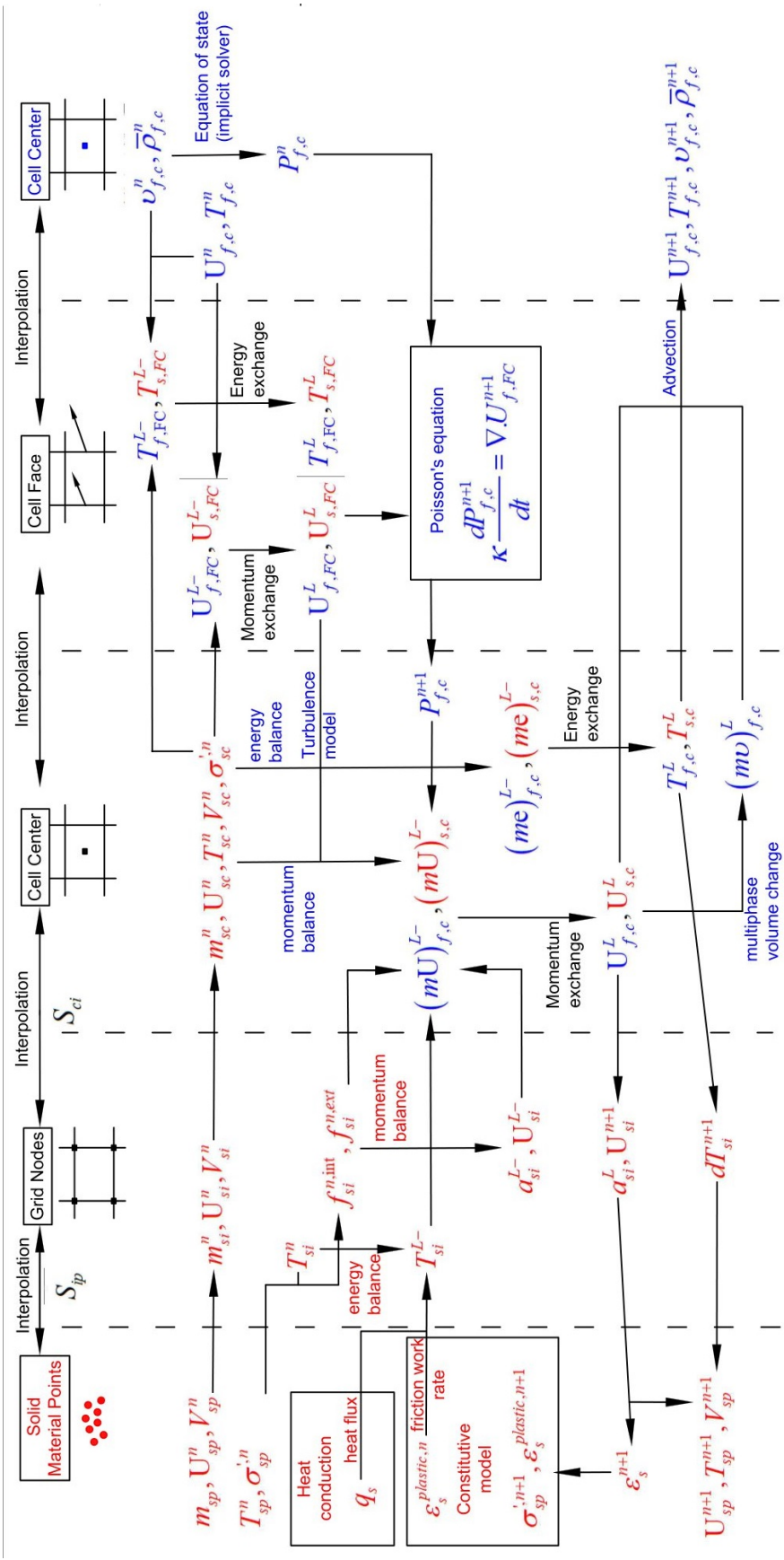


Figure 6: Numerical implementation of MPMICE

³²⁸ Then we compute the solid cell variables as:

$$\begin{aligned}
 m_{sc}^n &= \sum S_{ci} m_{si} \\
 \rho_{sc}^n &= \frac{m_{sc}^n}{V} \\
 \mathbf{U}_{sc}^n &= \sum S_{ci} \mathbf{U}_{si}^n \\
 T_{sc}^n &= \sum S_{ci} T_{si}^n \\
 V_{sc}^n &= \sum S_{ci} V_{si}^n \\
 \boldsymbol{\sigma}_{sc}^n &= \sum S_{ci} \boldsymbol{\sigma}_{si}^n
 \end{aligned} \tag{41}$$

³²⁹ *Compute equation of state for fluid phase*

³³⁰ The total fluid material volume of a cell is:

$$V_{total} = \sum_{f=1}^{N_f} M_f v_f \tag{42}$$

³³¹ We need to find $P_{f,c}^n$ which allows each fluid materials obey their equation of
³³² states $[P_f, \rho_f, v_f, T_f, e_f]$ but also allow mass of all fluid materials to fill the
³³³ entire the pore volume without ongoing compression or expansion following
³³⁴ the condition as follows:

$$0 = n - \sum_{f=1}^{N_f} v_f \bar{\rho}_f \tag{43}$$

³³⁵ Then, we can use the Newton-Raphson interation to find the value of $P_{f,c}^n$
³³⁶ which satisfies the equation (42, 43) and each equation of states of each fluid
³³⁷ materials.

³³⁸ *Compute cell face velocity*

³³⁹ Following the derivation in the Appendix: Advanced Fluid Pressure, we
³⁴⁰ first compute the fluid cell face velocity as:

$$\mathbf{U}_{f,FC}^{L-} = \frac{(\bar{\rho} \mathbf{U})_{f,FC}^n}{\bar{\rho}_{f,FC}^n} + \Delta t \left(-\frac{\nabla^{FC} P_{f,c}^n}{\bar{\rho}_{f,FC}^n} + \frac{\nabla^{FC} \cdot \boldsymbol{\tau}^n}{\bar{\rho}_{s,FC}} + \mathbf{b} \right) \tag{44}$$

³⁴¹ The equation (44) is discretized in three dimension (noted that $\nabla^{FC} \cdot \boldsymbol{\tau} = 0$),
³⁴² for example the discretized equation in the x direction is:

$$U_{fx}^{L-} = \frac{(\bar{\rho} U)_{fx,R}^n + (\bar{\rho} U)_{fx,L}^n}{\bar{\rho}_{fx,L}^n + \bar{\rho}_{fx,R}^n} + \Delta t \left(-\frac{2(v_{fx,L}^n v_{fx,R}^n)}{v_{fx,L}^n + v_{fx,R}^n} \frac{P_{f,cx,R}^n - P_{f,cx,L}^n}{\Delta x} + b_x \right) \tag{45}$$

³⁴³ The cell face solid velocity can be calculated as:

$$\mathbf{U}_{s,FC}^{L-} = \frac{(\bar{\rho}\mathbf{U})_{s,FC}^n}{\bar{\rho}_{s,FC}^n} + \Delta t \left(\frac{\nabla^{FC} \cdot \boldsymbol{\sigma}_c'^n}{\bar{\rho}_{s,FC}} - \frac{\nabla^{FC} P_{f,c}^n}{\rho_s} + \mathbf{b} \right) \quad (46)$$

³⁴⁴ The equation (46) is discretized in three dimension (noted that $\nabla^{FC} \cdot \boldsymbol{\sigma}_{ij} = 0$
³⁴⁵ with $i \neq j$), for example the discretized equation in the x direction is:

$$U_{sx}^{L-} = \frac{(\bar{\rho}U)_{sx,R}^n + (\bar{\rho}U)_{sx,L}^n}{\bar{\rho}_{sx,L}^n + \bar{\rho}_{sx,R}^n} + \Delta t \left(\frac{2(\sigma_{xx,R} - \sigma_{xx,L})}{(\bar{\rho}_{sx,L}^n + \bar{\rho}_{sx,R}^n)\Delta x} - \frac{P_{f,cx,R}^n - P_{f,cx,L}^n}{\rho_s \Delta x} + b_x \right) \quad (47)$$

³⁴⁶ Then, we compute the modified cell face velocity \mathbf{U}_{FC}^L considering the mo-
³⁴⁷ mentum exchange (see the Appendix: Momentum exchange with an implicit
³⁴⁸ solve) as follows:

$$\begin{aligned} \mathbf{U}_{f,FC}^L &= \mathbf{U}_{f,FC}^{L-} + \Delta \mathbf{U}_{f,FC} \\ \mathbf{U}_{s,FC}^L &= \mathbf{U}_{s,FC}^{L-} + \Delta \mathbf{U}_{s,FC} \end{aligned} \quad (48)$$

³⁴⁹ The linear equation below is solved to obtain the increment of velocity with
³⁵⁰ $i,j = 1 : N$ as:

$$\begin{vmatrix} (1 + \beta_{ij}) & -\beta_{ij} \\ -\beta_{ji} & (1 + \beta_{ji}) \end{vmatrix} \begin{vmatrix} \Delta \mathbf{U}_{i,FC} \\ \Delta \mathbf{U}_{j,FC} \end{vmatrix} = \begin{vmatrix} \beta_{ij}(\mathbf{U}_{i,FC}^{L-} - \mathbf{U}_{j,FC}^{L-}) \\ \beta_{ji}(\mathbf{U}_{j,FC}^{L-} - \mathbf{U}_{i,FC}^{L-}) \end{vmatrix}$$

³⁵¹ Compute cell face temperature

³⁵² Similar to the velocity, the faced temperature is computed, for example
³⁵³ in x direction, as:

$$\begin{aligned} T_{fx}^{L-} &= \frac{(\bar{\rho}T)_{fx,R}^n + (\bar{\rho}T)_{fx,L}^n}{\bar{\rho}_{fx,L}^n + \bar{\rho}_{fx,R}^n} \\ T_{sx}^{L-} &= \frac{(\bar{\rho}T)_{sx,R}^n + (\bar{\rho}T)_{sx,L}^n}{\bar{\rho}_{sx,L}^n + \bar{\rho}_{sx,R}^n} \end{aligned} \quad (49)$$

³⁵⁴ Then, we compute the modified cell face temperature T_{FC}^L considering the
³⁵⁵ energy exchange (see the Appendix: Momentum and energy exchange with
³⁵⁶ an implicit solver) as follows:

$$\begin{aligned} T_{f,FC}^L &= T_{f,FC}^{L-} + \Delta T_{f,FC} \\ T_{s,FC}^L &= T_{s,FC}^{L-} + \Delta T_{s,FC} \end{aligned} \quad (50)$$

³⁵⁷ The linear equation below is solved to determine the increment of velocity
³⁵⁸ with $i,j = 1 : N$ as:

$$\begin{vmatrix} (1 + \eta_{ij}) & -\eta_{ij} \\ -\eta_{ji} & (1 + \eta_{ji}) \end{vmatrix} \begin{vmatrix} \Delta T_{i,FC} \\ \Delta T_{j,FC} \end{vmatrix} = \begin{vmatrix} \eta_{ij}(T_{i,FC}^{L-} - T_{j,FC}^{L-}) \\ \eta_{ji}(T_{j,FC}^{L-} - T_{i,FC}^{L-}) \end{vmatrix}$$

359 ***Compute fluid pressure (implicit scheme)***

360 For single phase flow, the increment of the fluid pressure can be computed
361 as:

$$\kappa_f \frac{\Delta P}{dt} = \nabla^c \cdot \mathbf{U}_{f,FC}^{n+1} \quad (51)$$

362 For multi-phase flows, the increment of the fluid pressure of the mixture can
363 be computed as:

$$\kappa \frac{\Delta P}{dt} = \sum_{f=1}^{N_f} \nabla^c \cdot (\phi_{f,FC} \mathbf{U}_{f,FC})^{n+1} \quad (52)$$

364 where $\kappa = \sum_{f=1}^{N_f} (\phi_{f,FC} \kappa_f) / \sum_{f=1}^{N_f} (\phi_{f,FC})$. Then, the fluid pressure at cell
365 center is:

$$P_c^{n+1} = P_c^n + \Delta P_c^n \quad (53)$$

366 Finally, the cell face advanced fluid pressure is:

$$P_{FC}^{n+1} = \left(\frac{P_{c,L}^{n+1}}{\bar{\rho}_{f,L}^n} + \frac{P_{c,R}^{n+1}}{\bar{\rho}_{f,R}^n} \right) / \left(\frac{1}{\bar{\rho}_{f,L}^n} + \frac{1}{\bar{\rho}_{f,R}^n} \right) = \left(\frac{P_{c,L}^{n+1} \bar{\rho}_{f,R}^n + P_{c,R}^{n+1} \bar{\rho}_{f,L}^n}{\bar{\rho}_{f,L}^n \bar{\rho}_{f,R}^n} \right) \quad (54)$$

367 ***Compute viscous shear stress term of the fluid phase***

368 This part compute the viscous shear stress $\Delta(m\mathbf{U})_{f,c,\tau}$ for a single vis-
369 cous compressible Newtonian fluid and optionally shear stress induced by the
370 turbulent model.

371 ***Compute nodal internal temperature of the solid phase***

372 The nodal internal temperature rate is computed based on the heat con-
373 duction model as below:

$$dT_{si}^{L-} = \frac{(\Delta W_{si}^n + \Delta W_{fric,i}^n + \nabla^i \cdot \mathbf{q}_{si}^n)}{m_{si}^n c_v} \quad (55)$$

374 where $\Delta W_{si}^n = \boldsymbol{\sigma}' : \frac{D_s(\boldsymbol{\epsilon}_s^p)}{Dt}$ is the mechanical work rate computed from the
375 constitutive model with $\boldsymbol{\epsilon}_s^p$ is the plastic strain, $\Delta W_{fric,i}^n$ is the work rate
376 computed from the contact law due to the frictional sliding between solid
377 materials. The heat flux is $\mathbf{q}_s = \bar{\rho}_s \beta_s \nabla T_s$ with β_s being the thermal conduc-
378 tivity of the solid materials.

$$T_{si}^{L-} = T_{si}^n + dT_{si}^{L-} \quad (56)$$

379 *Compute and integrate acceleration of the solid phase*

380 After interpolating from material points to the nodes, the nodal acceleration
381 and velocity are calculated by:

$$\mathbf{a}_{si}^{L-} = \frac{\mathbf{f}_{si}^{int,n} + \mathbf{f}_{si}^{ext,n}}{m_{si}^n} + \mathbf{g} \quad (57)$$

382

$$\mathbf{U}_{si}^{L-} = \mathbf{U}_{si}^n + \mathbf{a}_{si}^{L-} \Delta t \quad (58)$$

383 *Compute Lagrangian value (mass, momentum and energy)*

384 For the fluid phase, the linear momentum rate, the energy rate are:

$$\Delta(m\mathbf{U})_{f,c} = V n_c^n \nabla^c P_c^{n+1} + \Delta(m\mathbf{U})_{f,c,\tau} + V \bar{\rho}_{f,c}^n g \quad (59)$$

385

$$\Delta(me)_{f,c} = V n_c^n P_c^{n+1} \nabla^c \cdot \mathbf{U}_{f,FC}^* + \nabla^c \cdot \mathbf{q}_{f,c}^n \quad (60)$$

386 The Lagrangian value of the mass, linear momentum and energy of fluid
387 phases without momentum exchange are:

388

$$m_{f,c}^L = V \bar{\rho}_{f,c}^n \quad (61)$$

389

$$(m\mathbf{U})_{f,c}^{L-} = V \bar{\rho}_{f,c}^n \mathbf{U}_{f,c}^n + \Delta(m\mathbf{U})_{f,c} \quad (62)$$

390

$$(me)_{f,c}^{L-} = V \bar{\rho}_{f,c}^n T_{f,c}^n c_v + \Delta(me)_{f,c} \quad (63)$$

391 For the solid phase, the Lagrangian value of the linear momentum and energy
392 of solid phase are:

393

$$m_{sc}^L = m_{sc}^n \quad (64)$$

394

$$(m\mathbf{U})_{sc}^{L-} = \sum S_{ci} m_{si}^n \mathbf{U}_{si}^{L-} + V(1 - n_c^n) \nabla^c P_{f,c}^{n+1} \quad (65)$$

395

$$(me)_{sc}^{L-} = \sum S_{ci} m_{si}^n T_{si}^L c_v \quad (66)$$

396 To consider the momentum exchange, the Lagrangian velocity is modified as:

$$\begin{aligned} \mathbf{U}_{f,c}^L &= \mathbf{U}_{f,c}^{L-} + \Delta \mathbf{U}_{f,c} \\ \mathbf{U}_{sc}^L &= \mathbf{U}_{sc}^{L-} + \Delta \mathbf{U}_{sc} \end{aligned} \quad (67)$$

397 where the cell-centered intermediate velocity can be calculated by:

$$\begin{aligned} \mathbf{U}_{f,c}^{L-} &= \frac{(m\mathbf{U})_{f,c}^{L-}}{m_{f,c}^L} \\ \mathbf{U}_{sc}^{L-} &= \frac{(m\mathbf{U})_{sc}^{L-}}{m_{sc}^L} \end{aligned} \quad (68)$$

396 And the increment of the velocity $\mathbf{U}_{f,c}$, $\Delta\mathbf{U}_{sc}$ can be computed by solving
 397 the linear equation with $i,j = 1 : N$ as:

$$\begin{vmatrix} (1 + \beta_{ij}) & -\beta_{ij} \\ -\beta_{ji} & (1 + \beta_{ji}) \end{vmatrix} \begin{vmatrix} \Delta\mathbf{U}_{i,c} \\ \Delta\mathbf{U}_{j,c} \end{vmatrix} = \begin{vmatrix} \beta_{ij}(\mathbf{U}_{i,c}^{L-} - \mathbf{U}_{j,c}^{L-}) \\ \beta_{ji}(\mathbf{U}_{j,c}^{L-} - \mathbf{U}_{i,c}^{L-}) \end{vmatrix}$$

398 To consider the energy exchange, the Lagrangian temperature is modified as:

$$\begin{aligned} T_{f,c}^L &= T_{f,c}^{L-} + \Delta T_{f,c} \\ T_{sc}^L &= T_{sc}^{L-} + \Delta T_{sc} \end{aligned} \quad (69)$$

399 where the cell-centered intermediate temperature can be calculated by:

$$\begin{aligned} T_{f,c}^{L-} &= \frac{(mT)_{f,c}^{L-}}{m_{f,c}^L c_v} \\ T_{sc}^{L-} &= \frac{(mT)_{sc}^{L-}}{m_{sc}^L c_v} \end{aligned} \quad (70)$$

400 And the increment of the velocity can be computed by solving the linear
 401 equation with $i,j = 1 : N$ as:

$$\begin{vmatrix} (1 + \eta_{ij}) & -\eta_{ij} \\ -\eta_{ji} & (1 + \eta_{ji}) \end{vmatrix} \begin{vmatrix} \Delta T_{i,c} \\ \Delta T_{j,c} \end{vmatrix} = \begin{vmatrix} \eta_{ij}(T_{i,c}^{L-} - T_{j,c}^{L-}) \\ \eta_{ji}(T_{j,c}^{L-} - T_{i,c}^{L-}) \end{vmatrix}$$

402 Finally, we obtain the cell-centered solid acceleration and temperature rate
 403 as:

$$d\mathbf{U}_{sc}^L = \frac{(m\mathbf{U})_{sc}^L - (m\mathbf{U})_{sc}^n}{m_{sc}^L \Delta t} \quad (71)$$

$$dT_{sc}^L = \frac{(me)_{sc}^L - (me)_{sc}^n}{m_{sc}^L c_v \Delta t} \quad (72)$$

405 Compute Lagrangian specific volume of the fluid phase

406 To compute the Lagrangian value of the specific volume of the fluid phase,
 407 we need to compute the Lagrangian temperature rate as below:

$$T_{f,c}^{n+1} = \frac{(me)_{f,c}^L}{m_{f,c}^L c_v} \quad (73)$$

$$\frac{D_f T_{f,c}}{Dt} = \frac{T_{f,c}^{n+1} - T_{f,c}^n}{\Delta t} \quad (74)$$

⁴⁰⁹ As such, the Lagrangian specific volume rate is:

$$\Delta(mv)_{f,c} = V f_{f,c}^\phi \nabla \cdot \mathbf{U} + (\phi_{f,c} \alpha_{f,c} \frac{D_f T_{f,c}}{Dt} - f_{f,c}^\phi \sum_{n=1}^N \phi_{nc} \alpha_{nc} \frac{D_n T_{n,c}}{Dt}) \quad (75)$$

⁴¹⁰ where $f_f^\phi = (\phi_f \kappa_f) / (\sum_{n=1}^N \phi_n \kappa_n)$ and $\mathbf{U} = \nabla \cdot (\sum_{s=1}^{N_s} \phi_{sc} \mathbf{U}_{sc} + \sum_{f=1}^{N_f} \phi_{fc} \mathbf{U}_{f,c})$.

⁴¹¹ Finally, the Lagrangian specific volume is:

$$(mv)_{f,c}^L = V \bar{\rho}_{f,c}^n v_{f,c}^n + \Delta(mv)_{f,c} \quad (76)$$

⁴¹² *Compute advection term and advance in time*

⁴¹³ The time advanced mass, linear momentum, energy and specific volume
⁴¹⁴ are:

$$m_{f,c}^{n+1} = m_{f,c}^L - \Delta t \nabla \cdot (\bar{\rho}_{f,c}^L, \mathbf{U}_{f,FC}^L) \quad (77)$$

$$(m\mathbf{U})_{f,c}^{n+1} = (m\mathbf{U})_{f,c}^L - \Delta t \nabla \cdot ((\bar{\rho}\mathbf{U})_{f,c}^L, \mathbf{U}_{f,FC}^L) \quad (78)$$

$$(me)_{f,c}^{n+1} = (me)_{f,c}^L - \Delta t \nabla \cdot ((\bar{\rho}c_v T)_{f,c}^L, \mathbf{U}_{f,FC}^L) \quad (79)$$

$$(mv)_{f,c}^{n+1} = (mv)_{f,c}^L - \Delta t \nabla \cdot ((\bar{\rho}v)_{f,c}^L, \mathbf{U}_{f,FC}^L) \quad (80)$$

⁴¹⁸ Finally, the state variables of the fluid phases of the next time step are:

$$\bar{\rho}_{f,c}^{n+1} = \frac{m_{f,c}^{n+1}}{V} \quad (81)$$

$$\mathbf{U}_{f,c}^{n+1} = \frac{(m\mathbf{U})_{f,c}^{n+1}}{m_{f,c}^{n+1}} \quad (82)$$

$$T_{f,c}^{n+1} = \frac{(me)_{f,c}^{n+1}}{m_{f,c}^{n+1}} \quad (83)$$

$$v_{f,c}^{n+1} = \frac{(mv)_{f,c}^{n+1}}{m_{f,c}^{n+1}} \quad (84)$$

422 *Interpolate from cell to node of the solid phase*

423 First we interpolate the acceleration, velocity and temperature rate to
 424 the node as below:

$$425 \quad \mathbf{a}_{si}^n = \sum S_{ci} d\mathbf{U}_{sc}^L \quad (85)$$

$$425 \quad \mathbf{U}_{si}^{n+1} = \sum S_{ci} d\mathbf{U}_{sc}^L \Delta t \quad (86)$$

$$426 \quad dT_{si}^n = \sum S_{ci} dT_{sc}^L \quad (87)$$

427 Then the boundary condition and contact forces f_{si}^{fric} are applied to the nodal
 428 velocity and the acceleration is modified by:

$$429 \quad \mathbf{a}_{si}^n = \frac{\mathbf{v}_{si}^{n+1} - \mathbf{v}_{si}^n}{\Delta t} \quad (88)$$

429 *Update the particle variables*

430 The state variables of the solid phase $[\mathbf{U}_{sp}^{n+1}, \mathbf{x}_{sp}^{n+1}, \nabla \mathbf{U}_{sp}^{n+1}, T_{sp}^{n+1}, \nabla T_{sp}^{n+1}, \mathbf{F}_{sp}^{n+1}, V_{sp}^{n+1}]$
 431 (velocity, position, velocity gradient, temperature, temperature gradient, de-
 432 formation gradient, volume) are updated as:

$$433 \quad \mathbf{U}_{sp}^{n+1} = \mathbf{U}_{sp}^n + \sum S_{sp} \mathbf{a}_{si}^n \Delta t \quad (89)$$

$$434 \quad \mathbf{x}_{sp}^{n+1} = \mathbf{x}_{sp}^n + \sum S_{sp} \mathbf{U}_{si}^{n+1} \Delta t \quad (90)$$

$$435 \quad \nabla \mathbf{U}_{sp}^{n+1} = \sum \nabla S_{sp} \mathbf{U}_{si}^{n+1} \quad (91)$$

$$436 \quad T_{sp}^{n+1} = T_{sp}^n + \sum S_{sp} dT_{si}^n \Delta t \quad (92)$$

$$436 \quad \nabla T_{sp}^{n+1} = \sum \nabla S_{sp} T_{sp}^n \Delta t \quad (93)$$

$$437 \quad \mathbf{F}_{sp}^{n+1} = (\mathbf{I} + \nabla \mathbf{U}_{sp}^{n+1} \Delta t) \mathbf{F}_{sp}^n \quad (94)$$

$$438 \quad V_{sp}^{n+1} = \det(\mathbf{F}_{sp}^{n+1}) V_{sp}^o \quad (95)$$

439 Finally, the effective stress $(\boldsymbol{\sigma}')^{n+1}$ is updated from the constitutive model
 440 and the pore water pressure is interpolated from the cell as:

$$439 \quad p_f^{n+1} = \sum S_{si} P_c^{n+1} \quad (96)$$

441 **Numerical examples**

442 All input files and the analytical calculations in this section are provided
 443 in the Github repository (https://github.com/QuocAnh90/Uintah_NTNU)
 444 for the reproduction of the numerical results.

445 To prevent repetition, we present the parameters of water and air, which
 446 remain consistent across all simulations. The water has a bulk modulus of 2
 447 GPa, a density of 998 kg/m³ at a reference temperature of 5 degrees Celsius
 448 and a reference pressure of 10325 Pa (1atm), a dynamic viscosity μ_f of 1
 449 mPa s). The air has a ideal gas with a density of 1.17 kg/m³ at a reference
 450 temperature of 5 degrees Celsius and a reference pressure of 10325 Pa (1atm),
 451 a dynamic viscosity μ_f of $18.45E^{-3}$ mPa s).

452 *Fluid Flow through isothermal porous media*

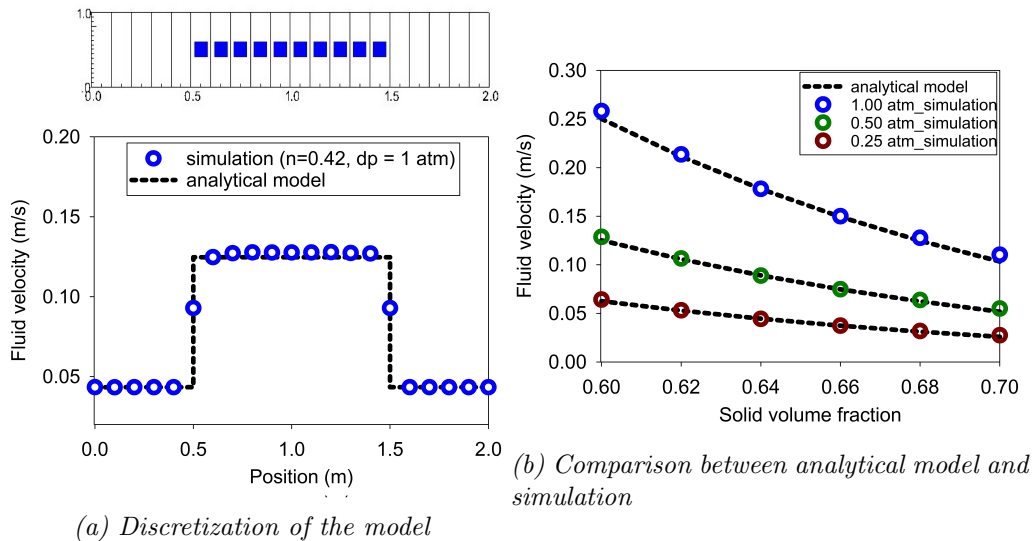


Figure 7: Numerical results of the fluid flow through isothermal porous media

453 Fluid flow through porous media is important in many engineering disci-
 454 plines, like predicting water flow in soil. Fluid flow velocity in one dimension
 455 can be calculated from the porous media's hydraulic conductivity K as:

456

$$U_f = K \frac{\Delta p_f}{L} \quad (97)$$

457 If the Carman-Kozeny formula is adopted $F = 10\phi_s/(1 - \phi_s)^2$, the hydraulic
 458 conductivity will be expressed as $K = D_p^2(1 - \phi_s)^3\rho_f g/180\phi_s^2\mu_f$. Then, the
 459 analytical formula of average velocity in one dimension through the porous
 460 media is:

461

$$U_f = \frac{1}{n} \frac{D_p^2(1 - \phi_s)^3}{180\phi_s^2\mu_f} \frac{\Delta p_f}{L} \quad (98)$$

462 Our numerical model is validated by modeling fluid flow through a 1m
 463 long porous media. The porous media is modeled by elastic material with
 464 Young's modulus is 10 MPa, Poisson's ratio is 0.3, and density is 2650 kg/m³.
 465 The volume fraction of porous media ϕ_s is [0.6, 0.62, 0.66, 0.68, 0.7] and the
 466 average grain diameter d is 1mm. The model is discretized in 20 finite element
 467 and the porous media in 10 finite element with 1 material point per element.
 468 The pressure gradient is applied with three different value [0.25, 0.5, 1] atm.
 469 Figure 7 shows a good agreement of fluid flow prediction between the theory
 470 and the model.

471 *Isothermal consolidation*

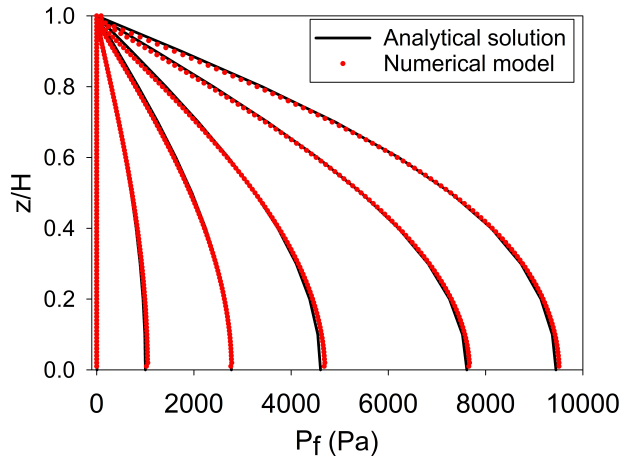


Figure 8: Comparison between analytical solution and numerical solution

472 A common benchmark for a fully saturated porous media is the simulation
 473 of one-dimensional consolidation. Using the Carman-Kozeny formula, the

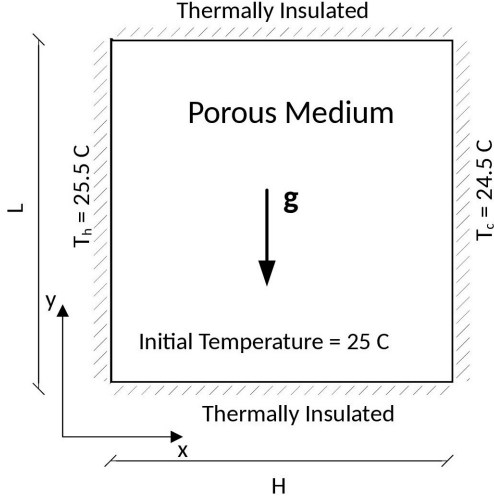


Figure 9: Model schematic [23]

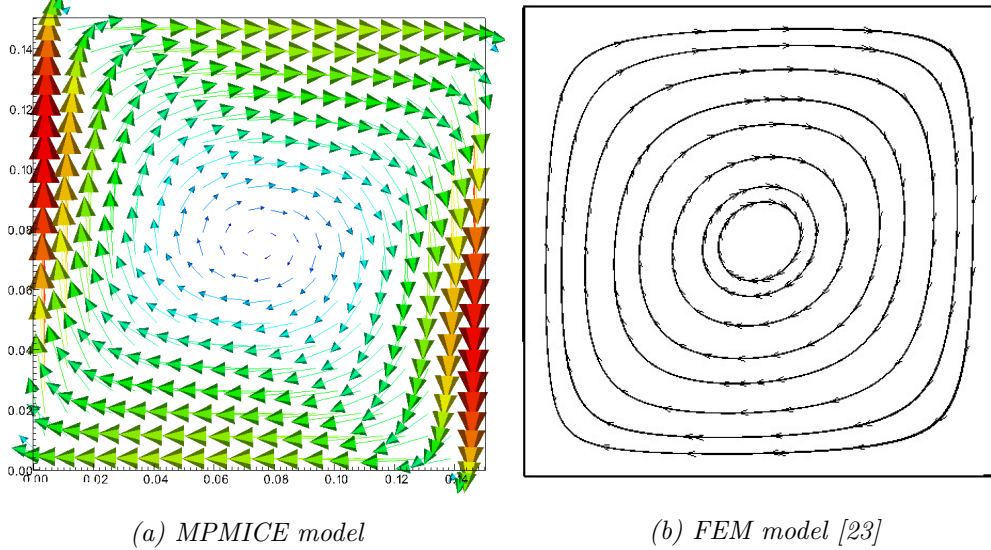
⁴⁷⁴ time-dependent pressure can be calculated as:

$$p_f = \sum_{m=1}^{\infty} \frac{2F_{ext}}{M} \sin\left(\frac{Mz}{H}\right) e^{-M^2 T_v} \text{ with } M = \frac{\pi}{2}(2m+1) \quad (99)$$

⁴⁷⁵ where the consolidation rate $T_v = C_v t / H^2$, the consolidation coefficient $C_v =$
⁴⁷⁶ $E_v n^3 d^2 / (180(1-n)^2 \mu)$ and the Oedometer modulus $E_v = E(1-v)/(1+v)/(1-2v)$. Our numerical model is validated by modeling the consolidation
⁴⁷⁷ of a 1m column. The porous media is modeled by elastic material with
⁴⁷⁸ Young's modulus is 10 MPa, Poisson's ratio is 0.3, and density is 2650 kg/m³.
⁴⁷⁹ The volume fraction of porous media ϕ_s is 0.7 which is equivalent to the
⁴⁸⁰ porosity of 0.3 and the average grain diameter d is 1mm. The model is
⁴⁸¹ discretized in 100 finite element with 1 material point per element. The
⁴⁸² external pressure applies to the top of the column is 10 kPa. Figure 8 shows
⁴⁸³ a good agreement of fluid flow prediction between the theory and the model.
⁴⁸⁴

⁴⁸⁵ *Thermal induced cavity flow*

⁴⁸⁶ Another benchmark is the thermal induced cavity flow in porous me-
⁴⁸⁷ dia. Temperature and velocity distributions are calculated for a square non-
⁴⁸⁸ deformable saturated porous media. The top and bottom walls are insulated,
⁴⁸⁹ and the left and right walls are at fixed temperature gradient of 1 degree.



(a) MPMICE model

(b) FEM model [23]

Figure 10: Comparison between MPMICE model and FEM model

490 The fluid motion at steady state are cavity flow due to the temperature in-
491duced density variation.

492 The numerical is validated by comparing with the numerical solution of the
493 finite element method. The porous media is modeled by non deformable ma-
494 terial, and density is 2500 kg/m³. The specific heat capacity of the water
495 and porous skeleton are 4181 J/kg.K and 835 J/kg.K respectively. The ther-
496 mal conductivity of the water and porous skeleton are 0.598 W/m.K and 0.4
497 W/m.K. The volume fraction of porous media ϕ_s is 0.6 which is equivalent
498 to the porosity of 0.4 and the average grain diameter d is 1mm. The model is
499 discretized in 20 x 20 finite element with 4 material point per element. Fig-
500 ure 10 shows a good agreement of numerical results of the model compared
501 with the numerical solution of the finite element method.

502 Underwater debris flow

503 The numerical example is validated by Rzadkiewicz et al.'s experiment
504 on submarine debris flow [24]. During the experiment, sand in a triangular
505 box is released and then slides along a rigid bed inclined 45 degrees under
506 water, see Figure 11.

507 In the numerical model, the material properties are selected based on the
508 experiment by Rzadkiewicz et al [24]. Sand has a saturated density of 1985

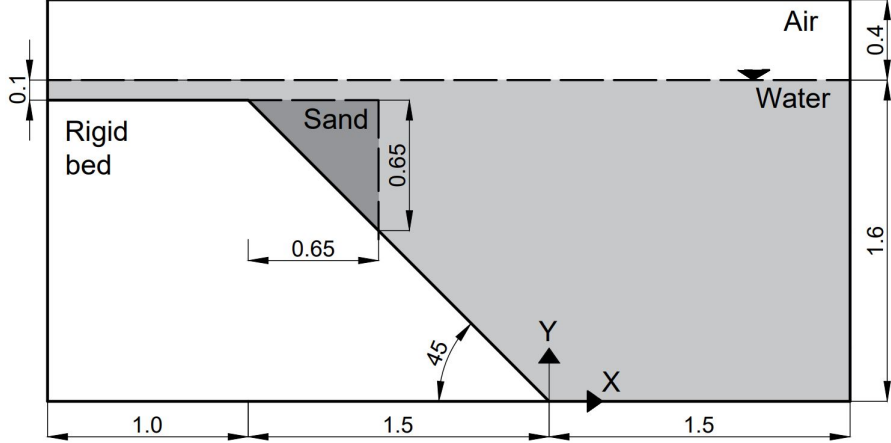


Figure 11: Model schematic

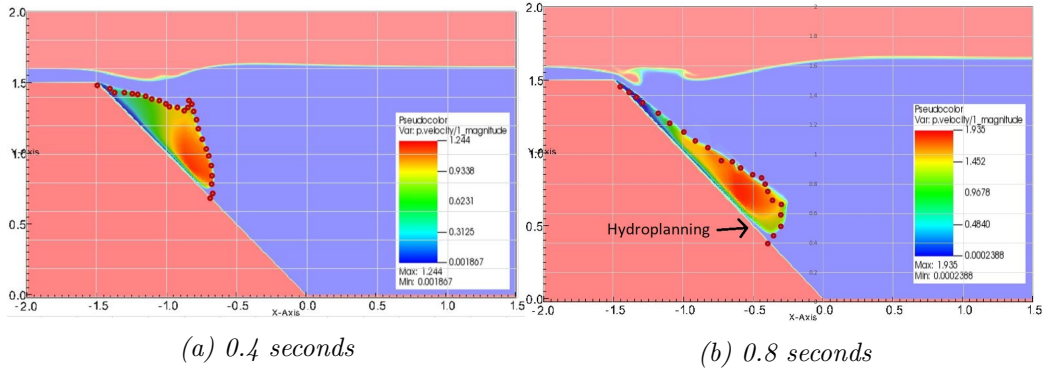


Figure 12: Simulation of underwater debris flow

509 kg/m^3 and yield stress of 200 Pa. Young's modulus has little effect on debris
 510 flow run-out because of the extreme large deformation of the debris. Therefore,
 511 we select 50 MPa Young's modulus with 0.25 Poisson's ratio. The rigid
 512 bed is much stiffer with bulk modulus and shear modulus of $117E^7$ Pa and
 513 $43.8E^7$ Pa. The numerical parameters used in this example are presented in
 514 Table 1.

515 On all boundary faces, the Dirichlet boundary condition is imposed for velocity
 516 ($u = 0$ m/s) and temperature ($T = 5$ Celcius degrees), while the Neuman
 517 boundary condition is imposed at the top boundary for pressure ($dp/dx = 0$
 518 kPa) and density ($d\rho/dx = 0$ kg/m^3). For the background mesh, there are
 519 $700 \times 400 = 280.000$ cells. In each cell of the debris flow and rigid bed, there

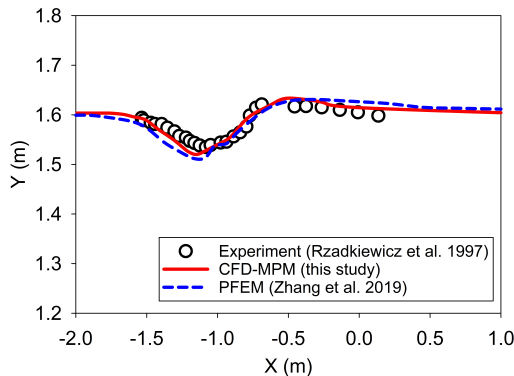
Materials	Bulk modul (Pa)	Shear modul (Pa)	Density (kg/m3)	Temp (C)	Dynamic viscosity (Pa s)	Yield stress (Pa)
Water (at surface)	2.15e9	-	999.8	5	855e-6	-
Air (at top boundary)	-	-	1.177	5	18.45e-6	-
Sand (porous media)	8.33e6	20e6	1985	5	-	200
Rigid bed (solid)	117e7	43.8e7	8900	5	-	-

Table 1: Numerical parameters for the underwater submarine debris

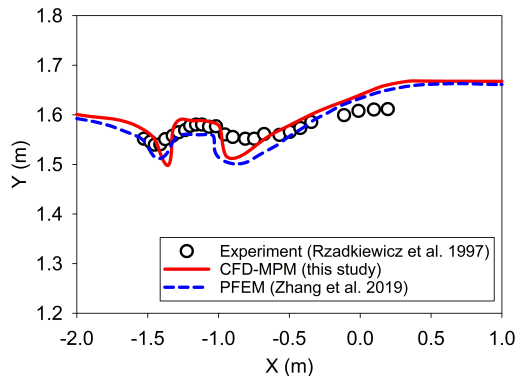
520 are 2 x 2 material points.

521 Figure 12a and 12b show snapshots of the debris flow sliding in the plane
 522 at 0.4 s and 0.8 s. Our simulations match the computed results from Rzad-
 523 kiewicz et al. [24]. The model also captures typical hydroplaning mechanism
 524 of the underwater debris flow (hydroplaning means the debris flow is lifted
 525 up and no longer in contact with the bottom layer). The elevation of the
 526 free surface at 0.4s and 0.8s is compared between our proposed method and
 527 other methods in Figure 13. Once again, our computed results were consis-
 528 tent with both the experiment and others computational results [7]. Unlike
 529 other computational models based on total stress analysis [5, 6, 7, 8], the
 530 proposed model based on the effective stress analysis which allows to analyze
 531 the water pressure and temperature in the debris flow.

532 We also explore the difference between underwater debris flow and sat-
 533 urated debris flow in terms of interacting with obstacle. Figure 14 shows the
 534 snapshot of the simulations of underwater and saturated debris flow. The
 535 saturated debris flow (see Figure 14a) behaves like frictional flow as grain
 536 have contact forces with each other. On the other hand, the underwater de-
 537 bris flow (see Figure 14b) behaves like turbulent flow as grains are separated
 538 from each other and exhibit no contact forces between grains.

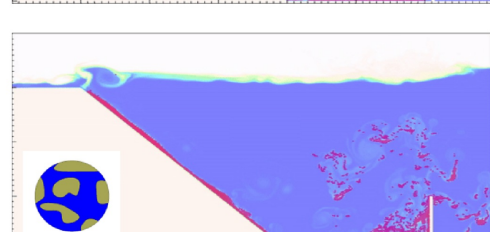
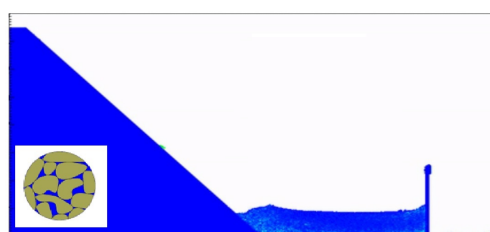
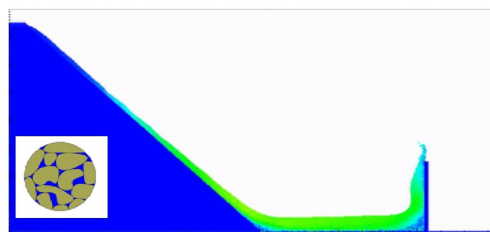
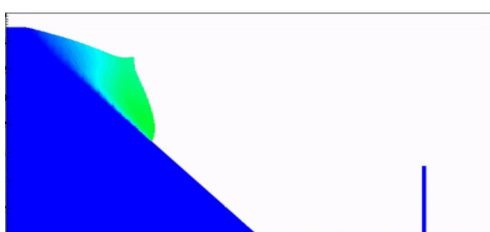


(a) 0.4 seconds



(b) 0.8 seconds

Figure 13: Simulation of underwater debris flow



(a) saturated debris flow using MPM

(b) underwater debris flow using MPMICE

Figure 14: Simulation of underwater debris flow

539 *Earthquake-induced submarine landslides*

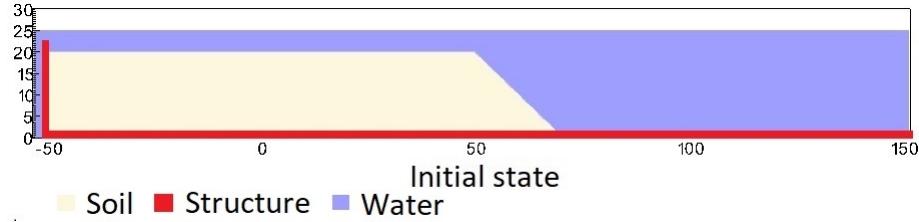


Figure 15: Numerical model of the earthquake-induced submarine landslide

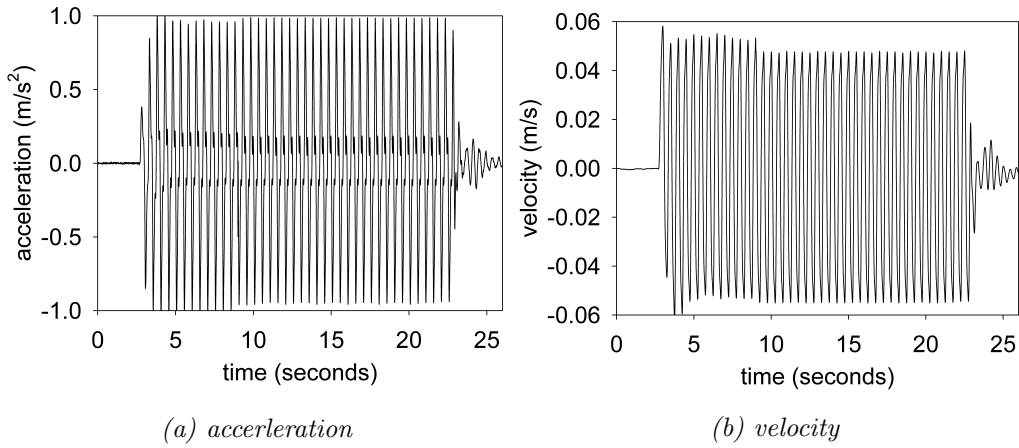


Figure 16: Ground acceleration profile, frequency of 2Hz and magnitude of 1g

540 In the final example, we perform numerical analysis of the earthquake
 541 induced submarine landslides. A plane strain model with the slope under
 542 water is shown in Figure 15. A 20m high slope with slope gradient of 45
 543 degrees is placed in a horizontal and vertical structure which was used to
 544 be a skaing table to apply earthquake loading. We simplify the earthquake
 545 loading by simulating the ground shaking for 20 seconds with the constant
 546 ground acceleration of 1g and a constant frequency of 2Hz (Figure 16a). The
 547 ground motion is applied in terms of velocity (Figure 16b). An earthquake
 548 of this magnitude is possible. For instance, in the case of the 2023 Turkey-
 549 Syria Earthquake, significant ground shaking with peak ground acceleration
 550 exceeding 1g was observed at numerous locations. This serves as an example

551 of the practical occurrence of such high levels of ground acceleration during
 552 seismic events.

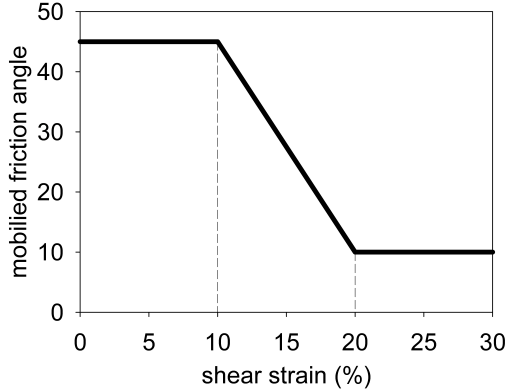


Figure 17: Mobilized friction angle in Mohr Coulomb model

553 A non-associated Mohr-Coulomb model is used for the soil. The soil grain
 554 has the density of 2650 kg/m^3 , Young's modulus of 10 kPa and Poisson's
 555 ratio of 0.3 and zero cohesion. The mobilized friction angle ϕ'_m is governed
 556 following the softening curve (see Figure 17) with the peak friction angle ϕ'_p
 557 of 45 degrees and the residual friction angle ϕ'_r of 10 degrees. The porosity
 558 is 0.3 and the average grain size of the soil is around $0.1 \mu\text{m}$ to mimic the
 559 undrained behavior. The mobilized dilatancy angle is calculated from the
 560 Rowe's stress dilatancy theory [25] as follow:

$$\sin \psi'_m = \frac{\sin \phi'_m - \sin \phi'_r}{1 - (\sin \phi'_r \sin \phi'_m)} \quad (100)$$

561 The solid plane is modeled as a rigid body acted as a shaking table. The
 562 contact between horizontal plane and the sand is the frictional contact with
 563 the friction coefficient of 0.1. No artificial damping is applied in the simu-
 564 lation. The contact between vertical plane and the sand is considered to be
 565 smooth with zero friction coefficient. On all boundary faces, the symmet-
 566 ric boundary condition is imposed, while the Neumann boundary condition
 567 is imposed at the top boundary for pressure ($d\rho/dx = 0 \text{ kPa}$) and density
 568 ($d\rho/dx = 0 \text{ kg/m}^3$). The mesh size is $0.25 \times 0.25 \text{ m}$ with 300852 element
 569 cells and 142316 material points. The simulation takes a couple of hours to
 570 perform 60 seconds of the simulation using 4096 CPUs.

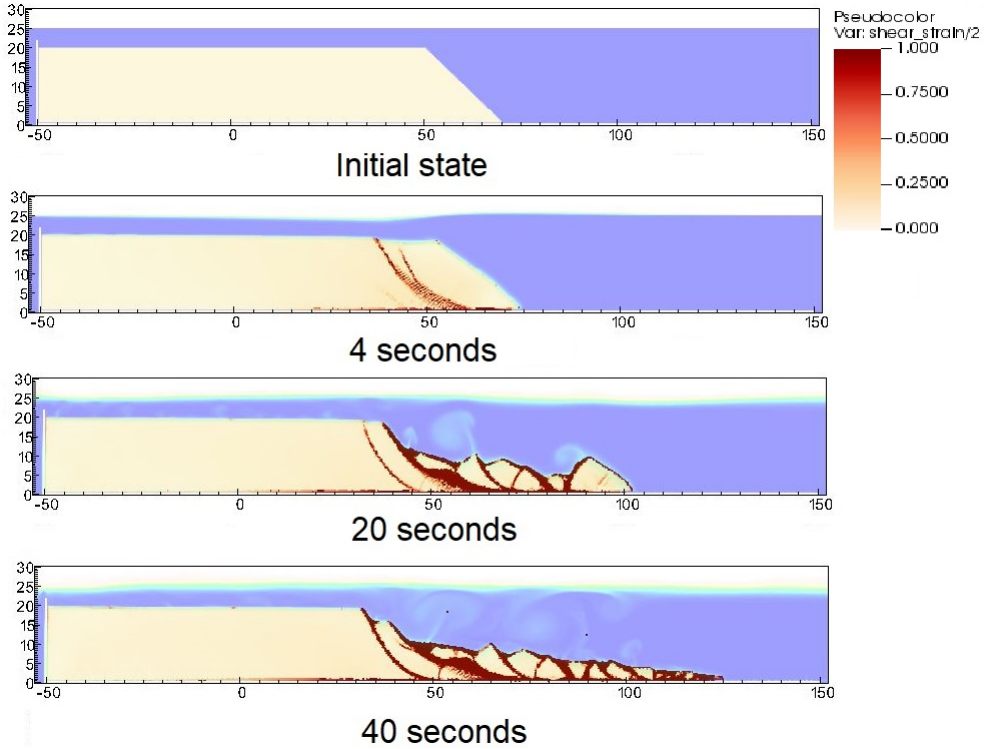


Figure 18: Shear strain during the earthquake-induced submarine landslides

571 We demonstrate the entire process and the mechanism of the earthquake-
 572 induced submarine landslides by showing the shear strain (Figure 18), the
 573 pore water pressure in atm (Figure 19) and the velocity (Figure 20). The
 574 failure mechanism can be characterized as the progressive failure mechanism.
 575 Here are some numerical observation:

- 576 1. At the initial of the seismic event, the seismic loading triggers the
 577 first slide at 3 seconds. At 4 seconds, the debris start to move with the
 578 maximum speed of around 2-3 m/s with multiple shear band developed
 579 in the slope. The wave generated from the submarine slide is around
 580 2-3m towards the slide direction.

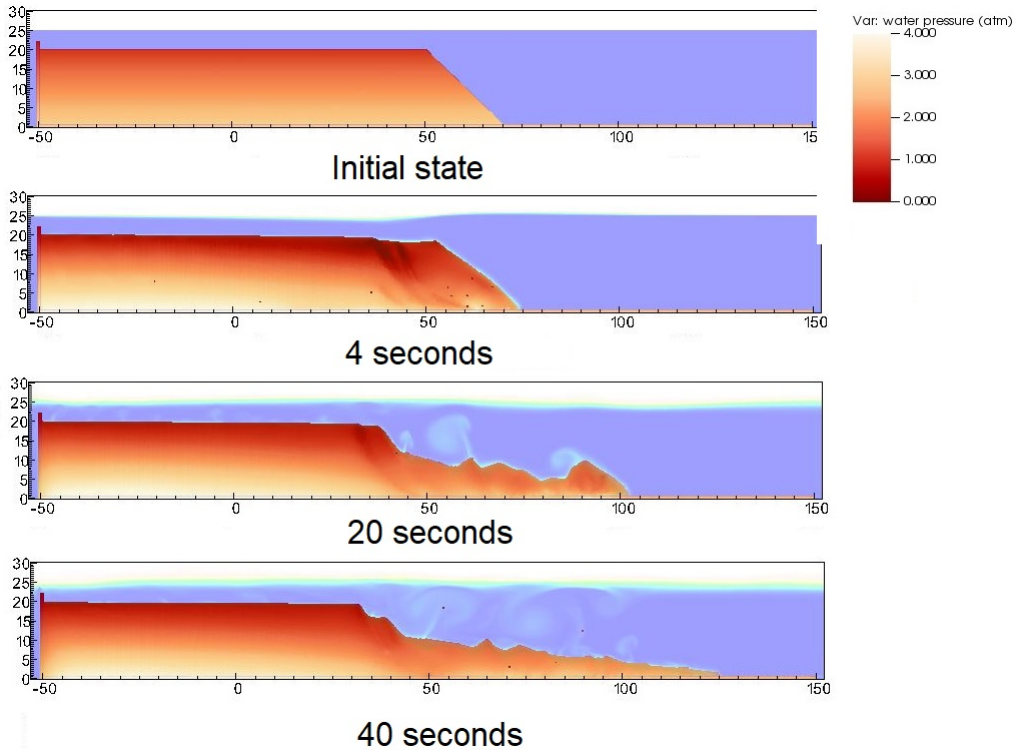


Figure 19: pore water pressure during the earthquake-induced submarine landslides

- 581 2. When the onset of the shear band occurs in the slope (for example
 582 at 4 seconds and 20 seconds), the negative excess pore water pressure
 583 is developed along this shear band with pore water pressure is under
 584 1atm. This is a typical dilatancy behavior when the soil is sheared
 585 rapidly in the undrained behavior.
- 586 3. When the seismic loading ends at 23 seconds, the last shear band is
 587 mobilized and the slope soon reaches to the final deposition. No more
 588 progressive failure developed in the slope. The turbulent flow developed
 589 as the interaction between debris flow and seawater.
- 590 Overall, we show the completed process of the earthquake-induced submarine
 591 landslides involving (1) earthquake triggering mechanism, (2) the onset of the
 592 shear band with the development of negative excess pore water pressure, (3)
 593 progressive failure mechanism, (4) submarine landslide induced wave to final
 594 deposition.

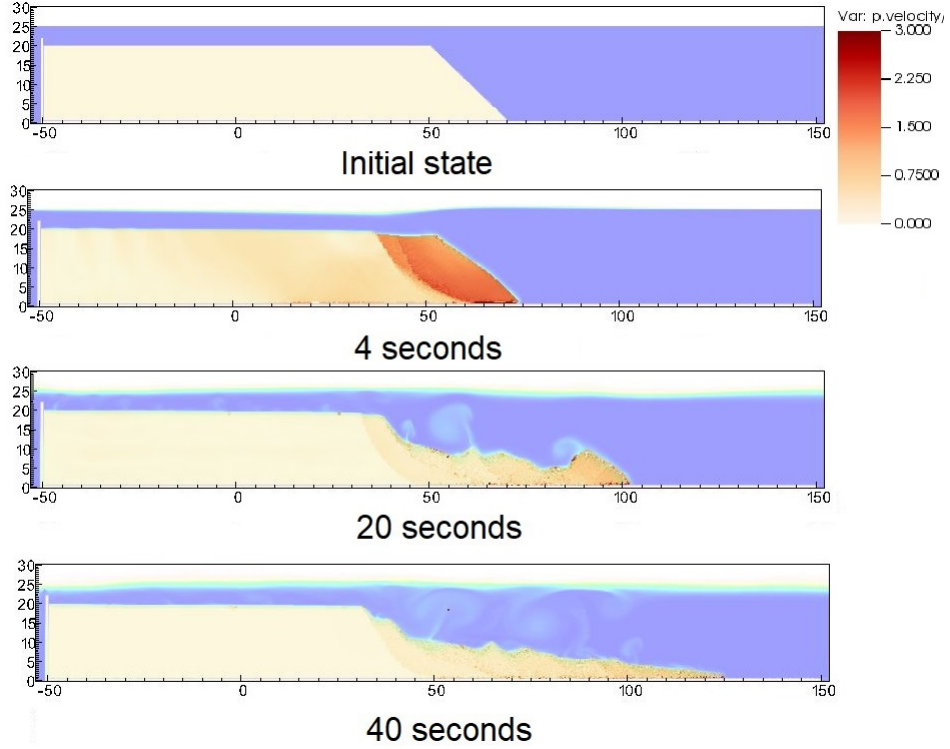


Figure 20: Velocity during the earthquake-induced submarine landslides

595 **Conclusions**

596 We have presented a numerical approach MPMICE for the simulation
 597 of large deformation soil-fluid-structure interaction, emphasizing the simu-
 598 lation of the earthquake-induced submarine landslides. The model uses (1)
 599 the Material Point Method for capturing the large deformation of iso-thermal
 600 porous media and solid structures and (2) Implicit Continuous Eulerian (com-
 601 pressible, conservative multi-material CFD formulation) for modeling the
 602 complex fluid flow including turbulence. This model is implemented in the
 603 high-performance Uintah computational framework and validated against an-
 604 alytical solution and experiment. We then demonstrate the capability of the
 605 model to simulate the entire process of the earthquake induced submarine
 606 landslides.

607 **Acknowledgements**

608 The authors gratefully acknowledge Dr. James Guilkey and Dr. Todd
 609 Harman from the University of Utah for sharing the insight on the theoretical
 610 framework of MPMICE which this work is based. This project has received
 611 funding from the European Union's Horizon 2020 research and innovation
 612 program under the Marie Skłodowska-Curie Actions (MSCA) Individual Fel-
 613 lowship (Project SUBSLIDE "Submarine landslides and their impacts on
 614 offshore infrastructures") grant agreement 101022007. The authors would
 615 also like to acknowledge the support from the Research Council of Norway
 616 through its Centers of Excellence funding scheme, project number 262644
 617 Porelab. The computations were performed on High Performance Comput-
 618 ing resources provided by UNINETT Sigma2 - the National Infrastructure
 619 for High Performance Computing and Data Storage in Norway.

620 **Appendix: Equation derivation**

621 Before deriving the governing equation, we define the Lagrangian deriva-
 622 tive for a state variable f as:

$$\frac{D_f f}{Dt} = \frac{\partial f}{\partial t} + \mathbf{U}_f \cdot \nabla f \quad \frac{D_s f}{Dt} = \frac{\partial f}{\partial t} + \mathbf{U}_s \cdot \nabla f \quad (101)$$

we use some definition following [16] as below:

$$-\frac{1}{V} \left[\frac{\partial V_f}{\partial p} \right] \equiv \kappa_f \quad \text{isothermal compressibility of fluid} \quad (102)$$

$$\frac{1}{V} \left[\frac{\partial V_f}{\partial T} \right] \equiv \alpha_f \quad \text{constant pressure thermal expansivity of fluid} \quad (103)$$

623 Then, the rate of volume with incompressible solid grains are calculated as
 624 belows:

$$\frac{1}{V} \frac{D_f V_f}{Dt} = \frac{1}{V} \left(\left[\frac{\partial V_f}{\partial p} \right] \frac{D_f P_{eq}}{Dt} + \left[\frac{\partial V_f}{\partial T_f} \right] \frac{D_f T_f}{Dt} \right) = \frac{1}{V} \left(-\kappa_f \frac{D_f P_{eq}}{Dt} + \alpha_f \frac{D_f T_f}{Dt} \right) \quad (104)$$

625 *Evolution of porosity*

626 Solving the solid mass balance equation (4) with the definition of solid
 627 mass in equation (2), it leads to the rate of porosity as belows:

$$\frac{D_s m_s}{Dt} = \frac{D_s (\phi_s \rho_s V)}{Dt} = \rho_s V \frac{D_s \phi_s}{Dt} + \phi_s V \frac{D_s \rho_s}{Dt} + \phi_s \rho_s \frac{D_s V}{Dt} = 0 \quad (105)$$

628 The soil grains are assumed to be incompressible, therefore, term 2 in the
 629 right hand side is zero. leading to:

$$V \frac{D_s \phi_s}{Dt} + \phi_s \frac{D_s V}{Dt} = 0 \quad (106)$$

630 Dividing all terms with V with the equation $\frac{1}{V} \frac{D_s V}{Dt} = \nabla \cdot \mathbf{U}_s$, it leads to:

$$\frac{D_s n}{Dt} = \frac{\partial n}{\partial t} + \mathbf{U}_s \cdot \nabla n = \phi_s \nabla \cdot \mathbf{U}_s \quad (107)$$

631 **Momentum conservation**

632 The linear momentum balance equations for the fluid phases based on
 633 mixture theory are:

634

$$\frac{1}{V} \frac{D_f(m_f \mathbf{U}_f)}{Dt} = \nabla \cdot (-\phi_f p_f \mathbf{I}) + \nabla \cdot \boldsymbol{\tau}_f + \bar{\rho}_f \mathbf{b} + \sum \mathbf{f}_d + \mathbf{f}_b \quad (108)$$

635 On the right hand sand, the first term is the divergence of partial fluid phase
 636 stress, the third term is the body force, the fourth term is the drag force
 637 (momentum exchange) and the fifth term is the buoyant force described in
 638 [26] for the immiscible mixtures. The buoyant force is in the form as belows:

$$\mathbf{f}_b = \boldsymbol{\sigma}_f \nabla(n) \quad (109)$$

639 As a result, the linear momentum balance equations for the fluid phases
 640 become as:

$$\frac{1}{V} \frac{D_f(m_f \mathbf{U}_f)}{Dt} = \frac{1}{V} \left[\frac{\partial(m_f \mathbf{U}_f)}{\partial t} + \nabla \cdot (m_f \mathbf{U}_f \mathbf{U}_f) \right] = -\phi_f \nabla p_f + \nabla \cdot \boldsymbol{\tau}_f + \bar{\rho}_f \mathbf{b} + \sum \mathbf{f}_d \quad (110)$$

641 The Reynolds stress component can be included in the term $\boldsymbol{\tau}_f$ to consider the
 642 turbulent effects if needed. To derive the linear momentum balance equation
 643 for the solid phase, we begin with the linear momentum balance equation for
 644 the mixture as:

$$\frac{1}{V} \frac{D_f(m_f \mathbf{U}_f)}{Dt} + \frac{1}{V} \frac{D_s(m_s \mathbf{U}_s)}{Dt} = \nabla \cdot (\boldsymbol{\sigma}) + \bar{\rho}_f \mathbf{b} + \bar{\rho}_s \mathbf{b} \quad (111)$$

645 Combining Terzaghi's equation (3) and subtracting both sides with equation
 646 (110), we obtain the linear momentum balance equations for the solid phase
 647 as:

$$\frac{1}{V} \frac{D_s(m_s \mathbf{U}_s)}{Dt} = \nabla \cdot (\boldsymbol{\sigma}') - \phi_s \nabla p_f + \bar{\rho}_s \mathbf{b} - \sum \mathbf{f}_d + \sum \mathbf{f}_{fric} \quad (112)$$

648 Here the \mathbf{f}_{fric} stems from the soil-structure interaction following the contact
 649 law between the soil/structure interfaces.

650 *Energy conservation*

651 We adopt the general form of the total energy balance equation for the
 652 porous media from [27], the total energy balance equations for the fluid phases
 653 are:

$$\frac{1}{V} \frac{D_f(m_f(e_f + 0.5\mathbf{U}_f^2))}{Dt} = \nabla \cdot (-np_f \mathbf{I}) \cdot \mathbf{U}_f + \nabla \cdot \mathbf{q}_f + (\bar{\rho}_f \mathbf{b}) \cdot \mathbf{U}_f + \sum \mathbf{f}_d \cdot \mathbf{U}_f + \sum q_{sf} \quad (113)$$

654 Applying the product rule $D(m\mathbf{U}^2) = D(m\mathbf{U} \cdot \mathbf{U}) = 2\mathbf{U} \cdot D(m\mathbf{U})$, the left
 655 hand side of equation (113) becomes:

$$\frac{1}{V} \frac{D_f(m_f(e_f + 0.5\mathbf{U}_f^2))}{Dt} = \frac{1}{V} \frac{D_f(m_f e_f)}{Dt} + \frac{1}{V} \frac{D_f(m_f \mathbf{U}_f)}{Dt} \cdot \mathbf{U}_f \quad (114)$$

657 Combining equations (110), (113), (114), we obtain the final form of the
 658 internal energy balance equation for the fluid phases as:

$$\frac{1}{V} \frac{D_f(m_f e_f)}{Dt} = \frac{1}{V} \left[\frac{\partial(m_f e_f)}{\partial t} + \nabla \cdot (m_f e_f \mathbf{U}_f) \right] = \bar{\rho}_f p_f \frac{D_f v_f}{Dt} + \nabla \cdot \mathbf{q}_f + \sum q_{sf} \quad (115)$$

659 On the right hand side, the terms include the average pressure-volume work,
 660 the average viscous dissipation, the thermal transport and the energy ex-
 661 change between solid and fluid respectively. The heat flux is $\mathbf{q}_f = \bar{\rho}_f \beta_f \nabla T_f$
 662 with β_f being the thermal conductivity coefficient. To derive the internal
 663 energy balance equation for the solid phase, we introduce the rate of the
 664 internal energy for the thermoelastic materials as a function of elastic strain
 665 tensor $\boldsymbol{\epsilon}_s^e$ and temperature T_s as belows:

$$\frac{m_s}{V} \frac{D_s(e_s)}{Dt} = \boldsymbol{\sigma}' : \frac{D_s(\boldsymbol{\epsilon}_s^e)}{Dt} + \frac{D_s(e_s)}{D_s(T_s)} \frac{D_s(T_s)}{Dt} = \boldsymbol{\sigma}' : \frac{D_s(\boldsymbol{\epsilon}_s^e)}{Dt} + c_v \frac{D_s(T_s)}{Dt} \quad (116)$$

666 c_v is the specific heat at the constant volume of the solid materials. The total
 667 energy balance equation for the mixture based on [27] can be written as:

$$\begin{aligned} & \frac{1}{V} \frac{D_f(m_f(e_f + 0.5\mathbf{U}_f^2))}{Dt} + \frac{1}{V} \frac{D_s(m_s(e_s + 0.5\mathbf{U}_s^2))}{Dt} = \nabla \cdot (-\phi_f p_f \mathbf{I}) \cdot \mathbf{U}_f \\ & + \nabla \cdot (\boldsymbol{\sigma}' - \phi_s p_f \mathbf{I}) \cdot \mathbf{U}_s + (-\phi_f p_f \mathbf{I}) : \nabla \mathbf{U}_f + \boldsymbol{\sigma}' : \nabla \mathbf{U}_s \\ & + (\bar{\rho}_f \mathbf{b}) \cdot \mathbf{U}_f + (\bar{\rho}_s \mathbf{b}) \cdot \mathbf{U}_s + \nabla \cdot \mathbf{q}_f + \nabla \cdot \mathbf{q}_s + \sum \mathbf{f}_d \cdot (\mathbf{U}_f - \mathbf{U}_s) \end{aligned} \quad (117)$$

669 Subtracting equation (117), (116) to equations (113) and (112), we obtained
670 the internal energy balance equation for solid phase as:

$$\boldsymbol{\sigma}' : \frac{D_s(\epsilon_s^e)}{Dt} + \frac{m_s}{V} c_v \frac{D_s(T_s)}{Dt} = \Delta W_s + \Delta W_{friction} + \nabla \cdot \mathbf{q}_s - \sum q_{sf} \quad (118)$$

671 On the right hand side, the terms include the work rate from frictional sliding
672 between solid materials $\Delta W_{friction}$, thermal transport and energy exchange
673 between solid and fluid respectively. The heat flux is $\mathbf{q}_s = \bar{\rho}_s \beta_s \nabla T_s$ with β_s
674 being the thermal conductivity of the solid materials, the mechanical work
675 rate $\Delta W_s = \boldsymbol{\sigma}' : \frac{D_s(\epsilon_s)}{Dt} = \boldsymbol{\sigma}' : (\frac{D_s(\epsilon_s^e)}{Dt} + \frac{D_s(\epsilon_s^p)}{Dt})$ computed from the constitutive
676 model with ϵ_s^p is the plastic strain tensor, . By subtracting the term $\boldsymbol{\sigma}' : \frac{D_s(\epsilon_s^e)}{Dt}$,
677 we get the final form of the energy balance equation as:

$$\frac{m_s}{V} c_v \frac{D_s(T_s)}{Dt} = \boldsymbol{\sigma}' : \frac{D_s(\epsilon_s^p)}{Dt} + \Delta W_{friction} + \nabla \cdot \mathbf{q}_s - \sum q_{sf} \quad (119)$$

678 Advanced Fluid Pressure

679 The discretization of the pressure equation begins with the Lagrangian
680 cell face velocity and the equation for the pressure as:

$$\bar{\rho}_{f,FC} \frac{\mathbf{U}_{f,FC}^{n+1} - \mathbf{U}_{f,FC}^n}{dt} = n \nabla^{FC} P_{f,c}^{n+1} + \bar{\rho}_{f,FC} \mathbf{b} \quad (120)$$

$$681 \quad \kappa \frac{dP}{dt} = \nabla^c \cdot \mathbf{U}_{f,FC}^{n+1} \quad (121)$$

682 The divergence of the equation (120) with $\nabla \cdot \mathbf{b} = 0$ is:

$$\nabla^c \cdot \mathbf{U}_{f,FC}^{n+1} - \nabla^c \cdot \mathbf{U}_{f,FC}^n = \nabla^c \frac{\Delta t}{\rho_{f,FC}^n} \cdot \nabla^{FC} (P_{f,c}^n + \Delta P_{f,c}^n) \quad (122)$$

683 To solve this equation, we define the cell face intermediate velocity $\mathbf{U}_{f,FC}^*$ as:

$$\bar{\rho}_{f,FC} \frac{\mathbf{U}_{f,FC}^* - \mathbf{U}_{f,FC}^n}{\Delta t} = n \nabla^{FC} P_{f,c}^n + \bar{\rho}_{f,FC} \mathbf{b} \quad (123)$$

684 The divergence of the equation (123) is:

$$\nabla^c \cdot \mathbf{U}_{f,FC}^* - \nabla^c \cdot \mathbf{U}_{f,FC}^n = \nabla^c \frac{\Delta t}{\rho_{f,FC}^n} \cdot \nabla^{FC} P_{f,c}^n \quad (124)$$

685 Combining equations (121, 122, 124), it leads to:

$$\left(\kappa - \nabla^c \frac{\Delta t}{\rho_{f,FC}^n} \cdot \nabla^{FC} \right) \Delta P_{fc}^n = -\nabla^c \cdot \mathbf{U}_{f,FC}^* \quad (125)$$

686 When the fluid is incompressible, κ approaches to zero and the equation
687 (125) becomes the Poisson's equation for the incompressible fluid flow.

688 *Momentum and Energy exchange with an implicit solver*

689 Considering the fluid momentum balance equation as:

$$(m\mathbf{U})_{f,FC}^{n+1} = (m\mathbf{U})_{f,FC}^n - \Delta t(Vn\nabla^{FC}P_{f,c}^n + m_f\mathbf{b}) + VK\Delta t(\mathbf{U}_{s,FC}^{n+1} - \mathbf{U}_{f,FC}^{n+1}) \quad (126)$$

690 And assuming $m_{f,FC}^{n+1} = m_{f,FC}^n$, we get:

$$\mathbf{U}_{f,FC}^{n+1} = \mathbf{U}_{f,FC}^n - \Delta t\left(\frac{\nabla^{FC}P_{fc}^n}{\rho_{f,FC}^n} + \mathbf{b}\right) + \frac{\Delta tK}{\bar{\rho}_{f,FC}^n}(\mathbf{U}_{s,FC}^{n+1} - \mathbf{U}_{f,FC}^{n+1}) \quad (127)$$

691 As defined in the section 'Advanced Fluid Pressure', the cell face intermediate
692 fluid velocity $\mathbf{U}_{f,FC}^* = \Delta t(\nabla^{FC}P_{fc}^n/\rho_{f,FC}^n + \mathbf{b})$ is computed as:

$$\mathbf{U}_{f,FC}^{n+1} = \mathbf{U}_{f,FC}^* + \frac{\Delta tK}{\bar{\rho}_{f,FC}^n}(\mathbf{U}_{s,FC}^{n+1} - \mathbf{U}_{f,FC}^{n+1}) \quad (128)$$

693 Considering the solid momentum balance equation as:

$$(m\mathbf{U})_{s,FC}^{n+1} = (m\mathbf{U})_{s,FC}^n - \Delta t(V\nabla^{FC} \cdot \boldsymbol{\sigma}'^n - V(1-n)\nabla^{FC}P_{f,c}^n + m_s\mathbf{b}) - VK\Delta t(\mathbf{U}_{s,FC}^{n+1} - \mathbf{U}_{f,FC}^{n+1}) \quad (129)$$

694 We define the cell face intermediate solid velocity as $\mathbf{U}_{s,FC}^* = \Delta t(\nabla^{FC} \cdot \boldsymbol{\sigma}'^n / \bar{\rho}_{s,FC}^n - \nabla^{FC}P_{f,c}^n/\rho_s + \mathbf{b})$ leading to:

$$\mathbf{U}_{s,FC}^{n+1} = \mathbf{U}_{s,FC}^* - \frac{\Delta tK}{\bar{\rho}_{s,FC}^n}(\mathbf{U}_{s,FC}^{n+1} - \mathbf{U}_{f,FC}^{n+1}) \quad (130)$$

696 Combining equation (128) and (130) we get:

$$\begin{aligned} \mathbf{U}_{f,FC}^* + \Delta\mathbf{U}_{f,FC} &= \mathbf{U}_{f,FC}^* + \frac{\Delta tK}{\bar{\rho}_{f,FC}^n}(\mathbf{U}_{s,FC}^* + \Delta\mathbf{U}_{s,FC} - \mathbf{U}_{f,FC}^* - \Delta\mathbf{U}_{f,FC}) \\ \mathbf{U}_{s,FC}^* + \Delta\mathbf{U}_{s,FC} &= \mathbf{U}_{s,FC}^* - \frac{\Delta tK}{\bar{\rho}_{s,FC}^n}(\mathbf{U}_{s,FC}^* + \Delta\mathbf{U}_{s,FC} - \mathbf{U}_{f,FC}^* - \Delta\mathbf{U}_{f,FC}) \end{aligned} \quad (131)$$

697 Rearranging the equation (131), it leads to the linear system of equations as
 698 belows:

$$\begin{vmatrix} (1 + \beta_{12,FC}) & -\beta_{12,FC} \\ -\beta_{21,FC} & (1 + \beta_{21,FC}) \end{vmatrix} \begin{vmatrix} \Delta \mathbf{U}_{f,FC} \\ \Delta \mathbf{U}_{s,FC} \end{vmatrix} = \begin{vmatrix} \beta_{12,FC}(\mathbf{U}_{s,FC}^* - \mathbf{U}_{f,FC}^*) \\ \beta_{21,FC}(\mathbf{U}_{f,FC}^* - \mathbf{U}_{s,FC}^*) \end{vmatrix}$$

699 Solving this linear equations with $\beta_{12,FC} = (\Delta t K) / \bar{\rho}_{f,FC}^n$ and $\beta_{21,FC} =$
 700 $(\Delta t K) / \bar{\rho}_{s,FC}^n$ with K is the momentum exchange coefficient. Similar deriva-
 701 tion can be performed to computed the cell-center velocity increment leading
 702 to:

$$\begin{vmatrix} (1 + \beta_{12c}) & -\beta_{12c} \\ -\beta_{21c} & (1 + \beta_{21c}) \end{vmatrix} \begin{vmatrix} \Delta \mathbf{U}_{f,c} \\ \Delta \mathbf{U}_{sc} \end{vmatrix} = \begin{vmatrix} \beta_{12c}(\mathbf{U}_{sc}^* - \mathbf{U}_{f,c}^*) \\ \beta_{21c}(\mathbf{U}_{f,c}^* - \mathbf{U}_{sc}^*) \end{vmatrix}$$

703 with $\beta_{12c} = (\Delta t K) / \bar{\rho}_{f,c}^n$ and $\beta_{21c} = (\Delta t K) / \bar{\rho}_{sc}^n$ and the cell-centered interme-
 704 diate velocity can be calculated by:

$$\begin{aligned} \mathbf{U}_{f,c}^* &= \mathbf{U}_{f,c}^n + \Delta t \left(-\frac{\nabla P_{f,c}^{n+1}}{\rho_{f,c}^n} + \frac{\nabla \cdot \boldsymbol{\tau}_{f,c}^n}{\bar{\rho}_{f,c}^n} + \mathbf{b} \right) \\ \mathbf{U}_{sc}^* &= \mathbf{U}_{sc}^n + \Delta t \left(\frac{\nabla \cdot \boldsymbol{\sigma}_c'^n}{\bar{\rho}_{sc}^n} - \frac{\nabla P_{f,c}^{n+1}}{\rho_s} + \mathbf{b} \right) \end{aligned} \quad (132)$$

705 For generalize multi materials i,j = 1:N, the linear equations is in the form
 706 as:

$$\begin{vmatrix} (1 + \beta_{ij}) & -\beta_{ij} \\ -\beta_{ji} & (1 + \beta_{ji}) \end{vmatrix} \begin{vmatrix} \Delta \mathbf{U}_i \\ \Delta \mathbf{U}_j \end{vmatrix} = \begin{vmatrix} \beta_{ij}(\mathbf{U}_i^* - \mathbf{U}_j^*) \\ \beta_{ji}(\mathbf{U}_j^* - \mathbf{U}_i^*) \end{vmatrix}$$

707 Similar approach applied for the ernergy exchange term leading to:

$$\begin{vmatrix} (1 + \eta_{ij}) & -\eta_{ij} \\ -\eta_{ji} & (1 + \eta_{ji}) \end{vmatrix} \begin{vmatrix} \Delta T_i \\ \Delta T_j \end{vmatrix} = \begin{vmatrix} \eta_{ij}(T_i^n - T_j^n) \\ \eta_{ji}(T_j^n - T_i^n) \end{vmatrix}$$

708 with η is the energy exchange coefficient.

709 References

- 710 [1] D. Yuk, S. Yim, P.-F. Liu, Numerical modeling of submarine mass-
 711 movement generated waves using RANS model, Computers and Geo-
 712 sciences 32 (7) (2006) 927–935. doi:10.1016/j.cageo.2005.10.028.
 713 URL <https://doi.org/10.1016/j.cageo.2005.10.028>

- 714 [2] S. Glimsdal, J.-S. L'Heureux, C. B. Harbitz, F. Løvholt, The 29th january 2014 submarine landslide at statland, norway—landslide dynamics,
715 tsunami generation, and run-up, *Landslides* 13 (6) (2016) 1435–1444.
716 doi:10.1007/s10346-016-0758-7.
717 URL <https://doi.org/10.1007/s10346-016-0758-7>
- 718 [3] S. Abadie, D. Morichon, S. Grilli, S. Glockner, Numerical simulation of waves generated by landslides using a multiple-fluid navier–stokes model, *Coastal Engineering* 57 (9) (2010) 779–794.
719 doi:10.1016/j.coastaleng.2010.03.003.
720 URL <https://doi.org/10.1016/j.coastaleng.2010.03.003>
- 721 [4] M. Rauter, S. Viroulet, S. S. Gylfadóttir, W. Fellin, F. Løvholt, Granular
722 porous landslide tsunami modelling – the 2014 lake askja flank collapse,
723 *Nature Communications* 13 (1) (Feb. 2022). doi:10.1038/s41467-022-
724 28296-7.
725 URL <https://doi.org/10.1038/s41467-022-28296-7>
- 726 [5] Q.-A. Tran, W. Sołowski, Generalized interpolation material point
727 method modelling of large deformation problems including strain-rate
728 effects – application to penetration and progressive failure problems,
729 *Computers and Geotechnics* 106 (2019) 249–265.
730 doi:10.1016/j.compgeo.2018.10.020.
731 URL <https://doi.org/10.1016/j.compgeo.2018.10.020>
- 732 [6] T. Capone, A. Panizzo, J. J. Monaghan, SPH modelling of water
733 waves generated by submarine landslides, *Journal of Hydraulic Research*
734 48 (sup1) (2010) 80–84. doi:10.1080/00221686.2010.9641248.
735 URL <https://doi.org/10.1080/00221686.2010.9641248>
- 736 [7] X. Zhang, E. Oñate, S. A. G. Torres, J. Bleyer, K. Krabbenhoft, A
737 unified lagrangian formulation for solid and fluid dynamics and its possi-
738 bility for modelling submarine landslides and their consequences, *Computer
739 Methods in Applied Mechanics and Engineering* 343 (2019) 314–
740 338. doi:10.1016/j.cma.2018.07.043.
741 URL <https://doi.org/10.1016/j.cma.2018.07.043>
- 742 [8] R. Dey, B. C. Hawlader, R. Phillips, K. Soga, Numerical modelling
743 of submarine landslides with sensitive clay layers, *Géotechnique* 66 (6)
- 744

- 747 (2016) 454–468. doi:10.1680/jgeot.15.p.111.
748 URL <https://doi.org/10.1680/jgeot.15.p.111>
- 749 [9] S. Bandara, K. Soga, Coupling of soil deformation and pore fluid flow
750 using material point method, Computers and Geotechnics 63 (2015)
751 199–214. doi:10.1016/j.compgeo.2014.09.009.
752 URL <https://doi.org/10.1016/j.compgeo.2014.09.009>
- 753 [10] A. P. Tampubolon, T. Gast, G. Klár, C. Fu, J. Teran, C. Jiang,
754 K. Museth, Multi-species simulation of porous sand and water
755 mixtures, ACM Transactions on Graphics 36 (4) (2017) 1–11.
756 doi:10.1145/3072959.3073651.
757 URL <https://doi.org/10.1145/3072959.3073651>
- 758 [11] A. S. Baumgarten, K. Kamrin, A general constitutive model for dense,
759 fine-particle suspensions validated in many geometries, Proceedings
760 of the National Academy of Sciences 116 (42) (2019) 20828–20836.
761 doi:10.1073/pnas.1908065116.
762 URL <https://doi.org/10.1073/pnas.1908065116>
- 763 [12] Q.-A. Tran, W. Sołowski, Temporal and null-space filter for the
764 material point method, International Journal for Numerical Methods in
765 Engineering 120 (3) (2019) 328–360. doi:10.1002/nme.6138.
766 URL <https://doi.org/10.1002/nme.6138>
- 767 [13] X. Zheng, F. Pisanò, P. J. Vardon, M. A. Hicks, An explicit stabilised
768 material point method for coupled hydromechanical problems in two-
769 phase porous media, Computers and Geotechnics 135 (2021) 104112.
770 doi:10.1016/j.compgeo.2021.104112.
771 URL <https://doi.org/10.1016/j.compgeo.2021.104112>
- 772 [14] Q. A. Tran, W. Sołowski, M. Berzins, J. Guilkey, A convected particle
773 least square interpolation material point method, International Journal
774 for Numerical Methods in Engineering 121 (6) (2019) 1068–1100.
775 doi:10.1002/nme.6257.
776 URL <https://doi.org/10.1002/nme.6257>
- 777 [15] J.-S. Chen, M. Hillman, S.-W. Chi, Meshfree methods: Progress made
778 after 20 years, Journal of Engineering Mechanics 143 (4) (Apr. 2017).

- 779 doi:10.1061/(asce)em.1943-7889.0001176.
780 URL [https://doi.org/10.1061/\(asce\)em.1943-7889.0001176](https://doi.org/10.1061/(asce)em.1943-7889.0001176)
- 781 [16] B. A. Kashiwa, A multifield model and method for fluid-structure in-
782 teraction dynamics, Tech. Rep. LA-UR-01-1136, Los Alamos National
783 Laboratory (2001).
- 784 [17] J. Guilkey, T. Harman, B. Banerjee, An eulerian-lagrangian
785 approach for simulating explosions of energetic devices,
786 Computers and Structures 85 (11) (2007) 660 – 674.
787 doi:<https://doi.org/10.1016/j.compstruc.2007.01.031>.
788 URL <http://www.sciencedirect.com/science/article/pii/S0045794907000429>
- 789 [18] A. S. Baumgarten, B. L. Couchman, K. Kamrin, A coupled finite volume
790 and material point method for two-phase simulation of liquid-sediment
791 and gas-sediment flows, Computer Methods in Applied Mechanics and
792 Engineering 384 (2021) 113940. doi:10.1016/j.cma.2021.113940.
793 URL <https://doi.org/10.1016/j.cma.2021.113940>
- 794 [19] S. Bardenhagen, J. Guilkey, K. Roessig, J. Brackbill, W. Witzel,
795 J.C.Foster, An improved contact algorithm for the material point
796 method and application to stress propagation in granular material,
797 CMES-Computer Modeling in Engineering and Sciences 2 (2001) 509–
798 522. doi:10.3970/cmes.2001.002.509.
- 799 [20] J. A. M. K. R. Beetstra, M. A. van der Hoef, Drag force of interme-
800 diate reynolds number flow past mono- and bidisperse arrays of spheres,
801 Fluid Mechanics and Transport Phenomena 53 (2) (2007) 489 – 501.
802 doi:<https://doi.org/10.1002/aic.11065>.
- 803 [21] R. W. Stewart, The air-sea momentum exchange, Boundary-Layer Me-
804 teorology 6 (1-2) (1974) 151–167. doi:10.1007/bf00232481.
805 URL <https://doi.org/10.1007/bf00232481>
- 806 [22] S. G. B. amd E. M. Kober, The generalized interpolation material point
807 method, Computer Modeling in Engineering and Sciences 5 (2004) 477–
808 496. doi:10.1016/j.compgeo.2021.104199.
809 URL <https://doi.org/10.3970/cmes.2004.005.477>
- 810 [23] S. G. Amiri, E. Taheri, A. Lavasan, A hybrid finite element model for
811 non-isothermal two-phase flow in deformable porous media, Computers

- 812 and Geotechnics 135 (2021) 104199. doi:10.1016/j.compgeo.2021.104199.
813 URL <https://doi.org/10.1016/j.compgeo.2021.104199>
- 814 [24] S. A. R. C. Mariotti;, P. Heinrich, Numerical simulation of sub-
815 marine landslides and their hydraulic effects, Journal of Waterway, Port,
816 Coastal, and Ocean Engineering 123 (4) (1997).
817 doi:[https://doi.org/10.1061/\(ASCE\)0733-950X\(1997\)123:4\(149\)](https://doi.org/10.1061/(ASCE)0733-950X(1997)123:4(149)).
- 818 [25] D. Muir Wood, Soil behaviour and critical state soil mechanics, Cam-
819 bridge University Press, United Kingdom, 1990.
- 820 [26] D. Drumheller, On theories for reacting immiscible mixtures, Interna-
821 tional Journal of Engineering Science 38 (3) (2000) 347 – 382.
822 doi:[https://doi.org/10.1016/S0020-7225\(99\)00047-6](https://doi.org/10.1016/S0020-7225(99)00047-6).
823 URL <http://www.sciencedirect.com/science/article/pii/S0020722599000476>
- 824 [27] S. Hassanzadeh, Derivation of basic equations of mass transport in
825 porous media, part1: Macroscopic balance laws, Advances in Wa-
826 ter Resources 9 (1986) 196–206. doi:[https://doi.org/10.1016/0309-1708\(86\)90024-2](https://doi.org/10.1016/0309-1708(86)90024-2).